UNIVERSITY OF CALIFORNIA

SANTA CRUZ

THREE-DIMENSIONAL SIMULATIONS OF FLUID AND HEAT FLOW ASSOCIATED WITH FAULTS IN VOLCANIC OCEAN CRUST

A thesis submitted in partial satisfaction
of the requirements for the degree of

MASTER OF SCIENCE

in

EARTH SCIENCES

by

Esther Adelstein

December 2017

The Thesis of Esther Adelstein
is approved:

Professor Andrew T. Fisher, Chair

Professor Francis Nimmo

Professor Slawek Tulaczyk

Tyrus Miller
Vice Provost and Dean of Graduate Studies

Table of Contents

ABSTRACT

THREE-DIMENSIONAL SIMULATIONS OF FLUID AND HEAT FLOW ASSOCIATED WITH FAULTS IN VOLCANIC OCEAN CRUST

Esther Adelstein

Hydrothermal circulation extracts a significant fraction of lithospheric heat from the ocean crust, with most of this advective heat loss occurring on ridge flanks, far from mid-ocean ridges. Faults in ocean crust are common in many settings, and may serve as high-transmissivity structures that facilitate advective transport and focus discharge of fluid, heat, and solutes below and at the seafloor. Coupled flow along fault zones has been invoked in a variety of settings, but circulation patterns are not well constrained by observational data or earlier models. We present results from three-dimensional, fully coupled numerical simulations of fluid and heat flow in sediment-covered ridge-flank ocean crust cut by a fault. We explore a range of fault and surrounding crustal characteristics, including crust and fault permeability, fault dip angle, thickness, and depth. We are particularly interested in resolving relations between fault and crustal characteristics and seafloor heat flux patterns.

Simulation results show variability in patterns of fluid circulation and seafloor heat flux as a function of fault geometry and crustal properties. The seafloor heat flux pattern above fault traces tends to show variability along strike (in response to underlying regions of rapid upward and downward flow along the fault trace), and asymmetry in seafloor heat flux anomalies, with higher values above the fault trace and lower values in the immediately surrounding seafloor, especially above the

hanging wall. The negative anomaly is generally greater when the fault dip angle is lower.

Higher permeability in the crustal rocks adjacent to the fault zone tend result in small-scale convection and small-amplitude variations in seafloor heat flux, and more diffuse convection cells in the fault zone itself. Convection in the surrounding crust decreases the importance of the fault zone in extracting lithospheric heat. Simulations also show that faults that penetrate deeper into the crust produce a significantly larger seafloor heat flux anomaly than do shallower faults, indicating that deeper faults extract lithospheric heat more efficiently. Patterns of seafloor heat flux from these simulations indicate that fault-zone hydrothermal circulation should produce thermal anomalies that are detectable in field measurements. Linking field observations directly to numerical simulations can provide better understanding of the geometry and properties of faults and fluid flow patterns in the volcanic ocean crust.

Three-dimensional simulations of fluid and heat flow associated with faults in volcanic ocean crust

1. Introduction

1.1 Background

Hydrothermal circulation extracts a significant fraction of lithospheric heat from the ocean crust and is responsible for the majority of the observed heat flow deficit compared to conductive global cooling models (Wolery and Sleep, 1976; Stein and Stein, 1994). Over 70% of this advective heat loss occurs on the flanks of mid-ocean ridges, in older crust and at lower temperatures than on-axis systems (Stein and Stein, 1992; Stein and Stein, 1994), equivalent to 4-7 TW in total (Hasterok 2013). Ridge-flank hydrothermal circulation drives significant solute fluxes between the crust and ocean (e.g., Elderfield and Schultz, 1996; Wheat and Mottl, 2004; Fisher and Wheat, 2010) and geochemical processes within the crust (e.g., Bach *et al.*, 2003; Alt, 2004; Boschi *et al.*, 2006). These flows support a vast and diverse biosphere in the uppermost volcanic basement and seafloor sediments (e.g., Amend and Teske, 2005; Edwards *et al.* 2005).

Global compilations of borehole bulk permeability measurements over a range of crustal ages indicate that the upper few hundred meters of ridge-flank volcanic basement tends to have high permeability compared to the relatively impermeable lower basement and overlying marine sediment (Fisher *et al.*, 2014; Spinelli *et al.*, 2004). This so-called "crustal aquifer" facilitates local and regional mixing and lateral

fluid flow over distances of tens of kilometers (e.g., Baker *et al.*, 1991; Hutnak *et al.*, 2006; Winslow and Fisher, 2015; Niera *et al.*, 2016). The coupled flows of fluid and heat in the volcanic ocean crust on ridge flanks are driven mainly by lithospheric heating from below. In addition to helping to explain the global heat flux anomaly on ridge flanks, coupled fluid-heat flow can also explain how heat is redistributed locally. The commonly observed positive correlation between heat flow and basement relief (i.e., high seafloor heat flow values located above basement highs) indicates isothermal conditions in upper basement associated with vigorous local convection (Davis *et al*. 1989; Fisher and Becker, 1995). Regional fluid flow that extracts heat and local fluid flow that redistributes heat can occur simultaneously, indicating the occurrence of mixed convection on many ridge flanks (e.g., Davis et al., 1992; Rosenberg et al., 2000; Stein and Fisher, 2003).

Heterogeneity or structures with different permeability may influence fluid and heat transport patterns in the volcanic crust on both local and regional scales. Faults are ubiquitous in ocean crust. Fault zones in a variety of settings have been characterized as conduits that facilitate hydrothermal fluid flow in the volcanic crust (e.g., Williams *et al*., 1979; Haymon *et al*., 1989; Delaney *et al*., 1992; Saccocia and Gillis, 1995; Villinger *et al.*, 2002; Coogan *et al*., 2006; McCaig *et al*., 2007; Hayman and Karson, 2009; Barker *et al*., 2010; Wheeler *et al*., 2013; Harris *et al*., 2017). The geometry and properties of fault zones should vary with both setting type and specific locations.

Detachment faults, low-angle extensional faults with large displacements, are characteristic features of slow-spreading ridges, especially near the intersection of extensional and transform plate boundaries (Smith *et al*., 2006; Cannat *et al.*, 2006; Cheadle and Grimes, 2010). Slip on detachment faults accompanies the uplift of oceanic core complexes, assemblages of lower crustal basaltic and gabbroic rocks and mantle peridotite. These are low-angle faults, with dips ranging from 15 to 45 degrees near the seafloor (Salisbury and Keen, 1993; Smith *et al.*, 2006; McCaig *et al.*, 2007) and sometimes steepening 3-4 km into the seafloor (Salisbury and Keen, 1993) (**Figure 1a**).

Hydrothermal activity is commonly associated with detachment faults and oceanic core complexes. The mineral assemblages along the detachment of the Atlantis Massif oceanic core complex indicate that fluid flow occurred along the fault zone during deformation (Escartin *et al*., 2003; Boschi *et al*., 2006). Studies of a detachment fault beneath the Trans-Atlantic Geotraverse (TAG) hydrothermal field on the Mid-Atlantic Ridge flank suggest that the fault focuses fluid flow and extracts heat from a deep source region. High-temperature fluids are thought to rise vertically from the shallow, low-angle portion of the fault through the fissured hanging wall (Tivey et al., 2003; Alt *et al.*, 2007; Canales *et al.*, 2007, DeMartin *et al.*, 2007). The majority of confirmed hydrothermal vent sites on the Mid-Atlantic Ridge flank are found above similar detachment faults (Andersen *et al*., 2015; Humphris *et al.*, 2015).

Subducting slabs of ocean crust also host faults with shallow to moderate dips. As an oceanic plate is subducted, the plate bends, forming a system of mostly

trenchward dipping extensional faults between the outer rise of the plate and the trench axis (Ludwig *et al*., 1966; Ranero *et al*., 2005; Naliboff *et al*., 2013) (**Figure 1b**). Seismic images and focal mechanisms of intraslab earthquakes indicate that outer-rise faults dip between 45° and 60° (Ranero *et al*., 2005). Outer-rise faults are thought to penetrate down through the crust and into the mantle to depths at some locations, perhaps penetrating to 18-20 kmbsf (Ranero *et al*., 2003). It has been suggested that these faults have sufficiently high permeabilities to allow hydrothermal activity; outer-rise faults are hypothesized to facilitate percolation of seawater through the lower crust and into the upper mantle, resulting in hydration and serpentinization of these deep regions (Peacock, 2001; Ranero *et al*., 2003; Faccenda *et al*., 2009). Such processes, if pervasive, would be significant for global geochemical fluxes.

Ocean crust below much of the seafloor is cut by faults associated with extension and the development of abyssal hills, which are among the most abundant geomorphic features on Earth (e.g., Kappel and Ryan, 1986; Macdonald *et al.*, 1996). Abyssal hill axes are oriented perpendicular to spreading direction and are bounded on the ridge side by normal faults that, in general, dip steeply near the surface (60° to 90°) and may have shallower dips (45° to 80°) at depth (Macdonald *et al.*, 1985 and 1996) (**Figure 1c**). On the non-ridge side, hills are bounded by volcanic growth faults, normal faults with similarly steep dips that penetrate 1-3 kmbsf (Dilek *et al.*, 1998). Coupled heat and fluid flow within abyssal hill fault zones has been invoked to explain the location of warm hydrothermal springs on the Juan de Fuca Plate (Mottl *et*

al., 1998). Johnson *et al*. (1993) suggested that a two-dimensional pattern of inter- and intra-fault hydrothermal circulation beneath abyssal hills could explain anomalous peaks in seafloor heat flux on the Juan de Fuca Ridge flank. There is also mineralogical and biological evidence for hydrothermal circulation in East Pacific Rise abyssal hill faults (Benjamin *et al*., 2006; Haymon *et al.*, 2005, Ehrhardt *et al*., 2007).

High-angle faults are also associated with fracture zones, which accommodate spreading along offset segments of mid-ocean ridges. On and near spreading axes, strike-slip motion on transform faults produces near-vertical planes of altered, relatively high-porosity and (hypothesized) high-permeability material (Karson *et al*., 2002; Hekinian, 2014) (**Figure 1d**). As spreading progresses, transform structures are displaced farther off axis and become seismically inactive; these structures continue for hundreds of kilometers beyond the ridge (Hekinian, 2014) and may provide extensive conduits for focusing fluid flow. Fluid flow through transform faults is thought to feed hydrothermal vents at both slow- (Bach et al., 2002; Baker et al., 2004) and fast-spreading ridges (Barker et al., 2010). Mineral assemblages indicate extensive hydrothermal circulation in fracture zones (e.g., Rona et al., 1987; Varnavas et al., 1988; Hart et al., 1990; Hayman and Karson, 2002).

The hydrogeology of fault zones in continental settings is somewhat better studied than that in the seafloor, but most earlier work has focused on specific settings rather than systematically exploring the potential influence of parameters such as fault angle, thickness, and properties in combination. Three-dimensional

modeling studies of hydrothermal flow on inclined faults are scarce and tend to be limited to site-specific studies (e.g., Cherubini *et al.*, 2013a; Cherubini *et al.*, 2014) or simulations of vertical or horizontal fault planes (Fairley, 2009; Pearson *et al.*, 2012; Cherubini *et al.*, 2013b). Two-dimensional models by Lopez and Smith (1995; 1996) studied the effects of topography and anisotropic and heterogeneous fault permeability on circulation patterns in a homogeneous, vertical fault zone. Ju and Yang (2011) explored a narrow (20°) range of fault dip angles in a study of fluid flow in two-dimensional models of ore formation at a site in Southern China.

1.2 Motivation

Hydrothermal circulation associated with faults is clearly important in the ocean crust, and likely occurs in a variety of settings having a wide range of system properties, geometries, and driving forces. This study comprises an initial step towards a comprehensive understanding of the influence of faults on hydrothermal processes in the ocean crust. We are specifically interested in fault-guided hydrothermal circulation in the ridge-flank setting, with a single fault and an idealized system geometry. We explore the influence of fault geometry and hydrogeologic properties on circulation patterns and seafloor heat flux.

A variety of observations of heat and fluid flow in ridge-flank ocean crust have been attributed to circulation facilitated by fault zones. Since faults are common on ridge flanks, processes associated with fault-zone hydrothermal circulation may be significant for heat extraction and redistribution in the upper crust on both global and local scales. The dynamics of fault-zone hydrothermal systems are poorly constrained

for several reasons: fault zone geometry is variable and difficult to observe, hydrologic properties of faults in ocean crust are not well constrained and values measured in situ do not necessarily hold over the scale of the entire system, and large-scale circulation patterns often cannot be resolved with field measurements alone.

There are few numerical modeling studies of hydrothermal circulation in faulted ridge-flank crust, and none have explored the effects of variations in hydrogeologic properties and geometry on circulation patterns and seafloor heat flux signals. Yang *et al.* (1996) ran two-dimensional simulations of hydrothermal circulation in ridge-flank crust cut by a series of horizontal and vertical fractures, inferring that fluid flow through fractures is required to produce the small-scale, ~1000 m wavelength heat flow variations measured on a transect along the Juan de Fuca Ridge flank by Davis *et al*. (1992). Subsequent two-dimensional modeling by Yang (2002) found that circulation guided by a series of normal faults dipping at 45° with hydraulic conductivity fixed at 10 times that of the surrounding basement produced significantly different seafloor heat flux signals than those from topography-governed circulation alone when faults penetrated upward through the sediment to the seafloor. When faults were buried beneath 100-250 m of sediment, seafloor heat flow variations were completely controlled by basement topography, despite significant fluid migration along the faults. Calculations for lateral flow in a two-dimensional crustal aquifer (Fisher and Becker, 2000) indicate that most of the fluid flow in the upper crust must be channelized through features such as faults and basement outcrops to match heat flow observations in relatively low-permeability

crust up to 65 Myr old, but the role of faults in facilitating vigorous circulation in the ocean crust is unclear.

We present results from the first three-dimensional simulations of hydrothermal circulation associated with an idealized fault cutting through volcanic ocean crust on a ridge flank. While we do not seek to simulate a particular field setting, the range of parameters we explore is guided by observations from specific field sites. The basic ocean crust model (described in greater detail in Section 2.2) is primarily based on ~2 to 5 Myr old seafloor on the eastern flank of the Juan de Fuca Ridge, an intermediate-rate spreading center (Davis *et al*., 1992; Davis *et al*., 1999; Hutnak et al., 2006). The hydrologic properties of the volcanic upper crust in this region have been studied more extensively than those in any other seafloor setting (e.g. Davis *et al*., 1997; Fisher *et al*., 2003; Wheat *et al*., 2004; Fisher et al., 2008; Mottl *et al*., 2008; Becker *et al*., 2013; Winslow *et al*., 2016; Niera *et al*., 2016).

Simulations of a generic ridge-flank fault are applied to address questions related to basic processes that could influence hydrothermal circulation in many settings (**Figure 1**):

(1) *What are the influences of fault geometry (angle, depth extent, thickness) on the efficiency and pattern of advective heat transfer?* In particular, do lower-angle faults mine a greater fraction of lithospheric heat than do higher-angle faults with characteristics that are otherwise similar due to the longer projection of low-angle faults on the horizontal (h_f, **Figure 2**)?

(2) *How do the magnitude of permeability and the contrast between crustal (bulk) and fault zone permeability influence coupled fluid-heat transport within a fault and the surrounding crust?* In particular, it may be that if crustal permeability is sufficiently high, convection outside of the fault zone can redistribute heat carried in the fault, reducing the magnitude of apparent anomalies associated with the fault zone.

(3) *How do the factors listed above influence the seafloor thermal signature of fault zone hydrogeology in the upper ocean crust?* This question is especially important for understanding the conditions under which thermal anomalies can be detected with seafloor measurements, and how these anomalies can be interpreted in terms of geologic structures and heat and fluid transport processes at depth.

2. Methods

2.1 Model domain and simulation configuration

This study uses Finite Element Heat and Mass (FEHM, version 3.2), a transient and fully coupled model of heat and mass transport developed at Los Alamos National Laboratory (Zyvoloski *et al*., 2011). FEHM uses the control-volume finite-element method, a node-centered finite-volume approach. FEHM solutions were calculated in this study using a fully implicit solver with upstream weighting.

Numerical domains are Delaunay meshes of tetrahedral elements constructed with Los Alamos Grid Toolbox (LaGriT) (George, 1997). The domain represents a simple section of ridge-flank crust with tabular layers: a crustal aquifer (extrusive volcanic rocks) underlain by conductive basement (sheeted dikes, gabbro) and

covered by a layer of lower permeability sediment. A fault zone cuts through the crustal aquifer and upper (otherwise conductive) basement layers (**Figure 3a**).

Properties are homogeneous in each unit, with the exception of the sediment layer, the properties of which are varied with depth to account for compaction. We run simulations with a range of fault dip angles (θ) fault permeability (k_f), and aquifer permeability (k_{aq}). We also vary fault thickness (t_f), aquifer thickness (t_{aq}), and fault penetration depth into basement (d_f). Dimensions and properties are guided by field observations and other numerical modeling results where available (as described in Section 2.2). The complete numerical mesh is a 6 km by 10 km (in map view) section of crust (**Figure 4).**

The fault zone is a high-resolution (node spacing <10 m) parallelepiped of nodes arranged in a regular isometric grid (**Figure 4a**). The nodes in the surrounding crust are connected in an irregular mesh of tetrahedra. Resolution is highest near the fault zone and decreases toward the edges of the domain (node spacing in the sediment and aquifer ranges from 50 to 200 m and in the conductive basement from 50 to 500 m). The thick conductive layer at the base of the domain (extending 3 km below the fault base) allows for warping of conductive isotherms in response to vigorous circulation in the fault and shallow basement while maintaining conductive conditions in the deep crust with constant basal heat flux.

The sides and bottom of the domain are adiabatic, no-flow boundaries. The top of the domain is held at a constant bottom-water temperature of 2 °C, as observed on the eastern flank of the Juan de Fuca Ridge (Davis *et al*., 1992; Hutnak *et al*.,

2006), and seafloor hydrostatic pressure. The base of the domain is a constant heat flow boundary and is closed to fluid flow. Basal heat input is 180 mW/m^2, the "background" heat flux for 3.4 - 3.6 Ma seafloor on the Juan de Fuca ridge flank (Hutnak *et al.*, 2006) (**Figure 3b)**. Water density, viscosity, and enthalpy are calculated for single-phase fluid using a pressure and temperature lookup table (Harvey *et al*., 1997) and bilinear interpolation (Zyvoloski *et al*., 2011) at each time step.

Simulations are run until a "dynamic steady state" is achieved, wherein heat input is nearly equal to heat output and primary circulation patterns have stabilized but transient behaviors may persist (e.g., unstable secondary convection). We consider a simulation to have reached dynamic steady state when total heat flux at the seafloor is within 3% of basal heat flux input. Internal balance errors calculated by FEHM are << 1%. Simulations are run for 10^5-10^6 years, with run times ranging from two to twelve weeks depending on permeabilities assigned to the crustal aquifer and fault zone. Initial conditions are generated in a two-step process. First, a conductive simulation is run to generate a thermal profile for initial temperature conditions. Next, we run a coupled simulation with moderate permeability in the aquifer and fault (k_f = $k_{aq} = 10^{-13}$ m^2, equal to the minimum permeability in final simulations) to allow convection patterns to develop. This background circulation pattern serves as the initial condition for higher permeability simulations. Our primary focus is on the dynamic-steady-state stable circulation patterns, and not their evolution.

2.2 Simulation parameter space

Though we do not aim to simulate a particular field site, we use the limited field data on faults in young ocean crust to guide our selection of rock properties and geologic unit dimensions (**Tables 1 and 2**). Borehole permeability tests conducted by Becker *et al.* (2013) in IODP Hole U1362A, also on the Juan de Fuca ridge flank, yielded bulk permeability values of 1-3 x 10^{-12} m^2 in the crustal aquifer. Cross-hole experiments in the region produced similar results for bulk permeability (Fisher *et al.*, 2008). In numerical simulations of seamount-guided hydrothermal flow in the same region, Winslow *et al.* (2016) found that an aquifer bulk permeability of 10^{-13}-10^{-12} m^2 yielded results that best matched field observations. We run simulations with k_{aq} = 10^{-13} and 10^{-12} m^2.

Properties for the fault zone are less well constrained. Becker *et al.* (1994) identified a thin high-permeability (10^{-10} m^2) zone at 610-615 mbsf in borehole packer tests in ODP Hole 857D in Middle Valley, a sedimented spreading center near the northern end of the Juan de Fuca Ridge. Based on seismic data in the region, they concluded that this structure is the intersection of the borehole with one of the major normal faults that bound abyssal hills in the region. We take 10^{-10} m^2 as an upper limit for k_f in our simulations; the measurement by Becker *et al.* may represent a highly transmissive fault zone core, meaning that the permeability of the fault zone conduit as a whole may be considerably lower. Additionally, 10^{-10} m^2 is approximately the highest permeability measured in other borehole packer tests in young crust (Fisher *et al.*, 2014).

Properties for sediment are varied with depth to account for compaction and are calculated using relationships derived from observations in fine-grained turbidites on the Juan de Fuca ridge flank (Spinelli *et al*., 2004). Sediment permeability is too low to permit thermally significant fluid flow through sediment, consistent with observations in this region (Giambalvo *et al*., 2000).

Fault zone thickness (t_f) is constrained by observations from escarpments in ~1-Ma-old crust exposed at the Hess Deep Rift, Cocos-Nazca spreading center (Hayman and Karson, 2007). In these in situ cross sections, fault cores and total fault damage zone widths are ~10 and <100 m, respectively. Seismic data and core samples on the Costa Rica Rift flank indicate that the volcanic growth faults that bound abyssal hills in the region extend to at least 1 km into basement (Dilek, 1998). Seismic studies of the detachment fault beneath the TAG geothermal field show that the fault dips shallowly to ~ 3 kmbsf into basement before steepening until its terminus at <7 kmbsf (DeMartin *et al.*, 2007). Global compilations of bulk permeability data (Fisher et al., 2014) suggest t_{aq} ~300 m, roughly corresponding to the upper extrusive volcanic complex. Numerical simulations by Winslow *et al*. (2016) indicate that t_{aq} on the Juan de Fuca ridge flank does not exceed 600 m. We use a constant sediment thickness of 250 m, a typical value for young seafloor of the eastern flank of the Juan de Fuca Ridge (Hutnak *et al.*, 2006).

We divide simulations into two groups (**Tables 2 and 3**). In the primary group, we vary θ between 30° and 90° for a 30-m thick fault that penetrates to a depth of 1 km, with a 300-m-thick aquifer intersecting the shallow part of the fault. For

each value of θ, we simulate coupled flows for six k_f - k_{aq} pairs. In the secondary group of simulations, we hold $\theta = 60°$ and explore variations in t_f (10 and 90 m), d_f (3 km), and t_{aq} (600 m) over a narrower range of permeabilities. We begin our presentation of results with a description of the results of a single reference simulation and use these observations to motivate metrics for analyzing the remaining simulations. Analyses are based on circulation patterns in the fault zone, the vigor with which the fault focuses flow, a comparison of flow rates in the fault zone and surrounding aquifer, and expressions of heat flux at the seafloor.

3. Results

3.1 Reference simulation and metrics

The reference simulation domain comprises a 30-m-thick, 1000-m-deep fault with a dip of 60° and a 300-m-thick aquifer. k_{aq} is 10^{-13} m^2 and k_f is 10^{-11} m^2. Fault thickness and dip are median values for our entire suite of simulations. The permeability contrast factor of 100 between the fault and aquifer is also an intermediate value.

The dynamic-steady-state temperature field (**Fig. 5**) shows a clear thermal signature related to the fault. The conductive profile is warped at the fault tips, with temperature lowered at the terminus of the fault in the conductive basement and elevated at the top of the fault at the sediment-basement interface, making the fault zone relatively isothermal compared to the conductive case (**Figure 5a**). There are three convection cells in the fault zone (three upwellings, four downwellings), oriented parallel to the fault plane (**Figure 5b**). There is convective overturn only

along strike, although the fault zone is defined perpendicular to dip with five layers of nodes. To quantify flow focusing along the fault plane, we interpolate the dip-parallel component of velocity on a plane oriented perpendicular to fault dip, halfway between the top and bottom of the fault (nominal intersection depth = 500 m below sediment-rock interface) (**Figure 6**).

The median up-dip (positive, dip-parallel) velocity ($\hat{u}_d$) in the fault at this depth is ~-10^{-8} m/s (~0.3 m/yr). Median total velocity magnitude in the fault (v_f) is ~10^{-7} m/s, six orders of magnitude greater than median total velocity magnitude in the aquifer (v_{aq} ~10^{-11} m/s). There is secondary convection in the aquifer, particularly close to the fault. Convective rolls in the aquifer are primarily oriented with axes in the y-direction, motion in the x-z plane, and velocities are negligible beyond ~1 km from the fault zone. There is no thermally significant fluid flow through the sediment.

There is a distinct positive anomaly in seafloor heat flux located along the fault trace (**Figure 7**). The thermal signature of convective upwellings and downwellings is visible as a series of peaks and troughs. There is a band of reduced heat flux located on the hanging wall, producing asymmetry in the heat flux signature at the seafloor. In the discussion of parametric variations that follows, we report the number of upwellings (a proxy for the number of convection cells), calculate $\hat{u}_d$, v_f, and v_{aq}, as described above, and show seafloor heat flux in map view.

3.2 Primary simulation results: dip angle and fault-aquifer permeability contrast

When $k_{aq} = 10^{-13}$ m^2, distinct circulation patterns form at most dip angles and persist at higher fault permeabilities (**Fig. 8**). There are two exceptions to this trend:

at $k_f = 10^{-13}$ m^2 for a dip angle of 30°, there is no convection in the fault zone, as is evident in the heat flux map (**Figure 8a)**. With no permeability contrast between the fault and aquifer and a fault protrusion into basement that is subparallel to the the aquifer because of the shallow dip angle, there is little difference between this geometry and the no-fault case. The other exception is the 90° dip case; at $k_f = 10^{-13}$ m^2, there are four distinct upwellings (**Figure 8q**), but this pattern shifts to two upwellings at the edges of the domain when $k_f = 10^{-12}$ to 10^{-10} m^2 (**Figure 8r-t**). For dip angles of 45° (**Figure 8e-h**), 60° (**Figure 8i-l**), and 75° (**Figure 8m-p**), the number of convection cells and their approximate x-y locations remain constant even as flow rates increase for higher k_f values, reducing the relief between heat flux peaks and troughs along the fault trace. The same consistency in convection "wavelength" is evident for the 30° dip angle case when $k_f = 10^{-12}$ to 10^{-10} m^2 (**Figure 8b-d**). Circulation in the 30°, 75°, and 90° faults is bounded by upwellings at both intersections of the fault with the edges of the domain, in the 60° fault by downwellings at both intersections, and in the 45° fault by one upwelling and one downwelling (**Figure 9**).

Earlier numerical simulations of fault zone hydrogeology (Zhao *et al.*, 2006) suggested that, if the permeability of a fault zone is three orders of magnitude higher than that of the surrounding rocks, fluid flow in the surrounding rocks and interaction with the fault zone is negligible. In order to investigate the stability of convection in the fault zone and confirm that convection should occur as observed, we approximate the Rayleigh number (*Ra*) for the vertical fault zone with $k_f = 10^{-10}$ m^2 and $k_{aq} = 10^{-13}$

m^2 when the system is convecting. If we assume that the top and bottom surfaces of the fault are isothermal, the Rayleigh number is defined as

$$Ra = \frac{\rho_f \alpha_f g \Delta T k h}{\mu \kappa_m} \quad \textbf{(1)}$$

where ρ_f is the density of the fluid, k is the permeability of the porous medium, α_f is the thermal expansivity of the fluid, ΔT is the temperature difference between the top and bottom of the fault, g is the gravitational constant, h is the height of the fault zone, κ_m is the thermal diffusivity of the fluid-saturated porous medium, and μ is the dynamic viscosity of the fluid (e.g., Ingebritsen *et al*., 2010). We use average fluid properties throughout the fault zone and average values for top and bottom temperatures at dynamic steady state for this Ra calculation (e.g., Wang *et al*., 1997). Ra = 1300 for a vertical fault zone with $k_f = 10^{-10}$ m^2 and h = 1 km, above the critical value of Ra (~1000) for the onset of convection in a thin, porous, vertical unit heated from below (Zhao *et al.*, 2008). For non-vertical faults, Ra is more difficult to calculate. Zhao *et al*. (2008) obtained numerical solutions for the critical value of Ra when $\theta < 90°$. For constant d_f, the critical value of Ra decreases with decreasing θ; a smaller value of θ results in an increase in along-dip length of the fault zone and therefore an increase in the amount of space in which convective fluid flow can occur. This destabilizing effect enables the onset of convection at less extreme conditions. It is therefore reasonable that convection occurs at lower dip angles with $k_f = 10^{-10}$ m^2 and $k_{aq} = 10^{-13}$ m^2, as observed. A smaller value of θ also results in a decrease of the gravity component along dip, reducing buoyancy in this direction and

hindering convection, but our results suggest along-dip buoyancy is sufficient to drive convection at lower angles.

When $k_{aq} = 10^{-12}$ m^2, there is significant convection in the aquifer (**Fig. 10**). This signal from aquifer convection cells is evident in variations in seafloor heat flux far from the fault trace. At $k_f = 10^{-12}$ m^2, the wavelength of convection is larger compared with the $k_{aq} = 10^{-13}$ m^2 case with equivalent k_f for dip angles of 30°, 45°, 60°, and 75° (**Figure 10a, c, e, g, i**). In all cases, though the upwelling heat flux peak value is not significantly lower, convection cells are more diffuse. There is higher relief between peaks and troughs in heat flux along the fault trace and wider peaks in heat flux that extend laterally beyond the fault trace. The number of upwellings decreases in all of the aforementioned cases except for 45° (**Figure 9**). At 45°, there is shift in "phase" of the convection cell pattern, and upwellings form at both edges of the domain. There is also a phase shift at 60°; circulation in the fault becomes bounded by one upwelling and one downwelling. The 45°, 75°, and 90° steady-state patterns are similar: three upwellings total, with upwellings at both edges of the domain (**Figure 10c, g, i**).

When k_f is increased to 10^{-11} m^2 for $k_{aq} = 10^{-12}$ m^2, convection patterns in the fault break down, forming two upwellings at the edge of the domain for most dip angles (**Figure 10b, d, f, h, j**). The exception is for a dip of 60°, where there is a phase shift from the lower k_f case, resulting in upwelling at one edge and downwelling at the other (**Figure 10e**). At $k_{aq} = 10^{-12}$ m^2 and $k_f = 10^{-11}$ m^2, any "characteristic" signal for a particular dip angle degrades into a large cell with size

apparently controlled by the boundaries of the domain (**Figure 9**). The size of the domain in the y-direction plays a role in governing convection cell size in these simulations. Nevertheless, the shift from multiple convection cells to a single large cell in the fault zone indicates a change in heat extraction regime as a function of the fault geometry and permeability contrast.

For $k_{aq} = 10^{-13}$ m^2, the median dip-parallel velocity ($\hat{u}_d$) increases with fault permeability for all fault angles (**Figure 11a**). For $k_{aq} = 10^{-12}$ m^2, such a trend is not apparent (**Figure 11b**). For $k_{aq} = 10^{-13}$ m^2 and $k_f = 10^{-12}$, 10^{-11}, 10^{-10} m^2, i.e., when circulation in the fault is much more significant than circulation in the aquifer, $\hat{u}_d$ decreases with increasing θ for $\theta > 60°$. $\hat{u}_d$ is highest for the 45° fault for all values of k_f except $k_f = 10^{-12}$, where $\hat{u}_d$ is highest at 60°. For all values of k_f, the magnitude of $\hat{u}_d$ at 90° is lower relative to that at lower angles, as is the interquartile range of $\hat{u}_d$ (**Figure 11a**).

Based on visual inspection of frequency histograms of $\hat{u}_d$ for all simulations, the distribution of up-dip velocity is unimodal and skewed toward positive values. For $k_{aq} = 10^{-13}$ m^2, the interquartile range of $\hat{u}_d$ increases with increasing k_f (**Figure 11a**). Fast up-dip flow is concentrated in upwelling zones, which account for less total area than do downwelling zones and convection cell centers (little-to-no along-dip flow) combined.

To further investigate the influence of permeability in the aquifer (k_{aq}) on circulation in the fault, we compare the median total velocity magnitude in the fault (v_f) with that in the aquifer (v_{aq}) for each permeability contrast factor (k_f/k_{aq}) (**Figure**

12). The ranges of v_{aq} and v_f are ~3 orders of magnitude for zero permeability contrast, but these ranges tighten considerably when permeability contrast factor is increased to 10. As the permeability contrast factor increases from 10 to 10^3, v_f increases by ~1 order of magnitude. Spearman's rank correlation coefficient (R_f, a nonparametric measure of how well the dependence between two variables can be described by a monotonic function) for v_f and k_f/k_{aq} >1 is 0.98. This is indicative of a positive correlation significant at the .05 level based on an exact permutation distribution test. Median total velocity in the fault increases with permeability contrast. Though v_{aq} for $k_f/k_{aq} > 1$ appears to be slightly lower compared to no-fault values (**Figure 12**), R_{aq} for v_{aq} and k_f/k_{aq} is -0.32, insignificant at the .05 level. For a 60° fault with $k_f = 10^{-11}$ m^2, an increase in aquifer permeability from 10^{-13} m^2 to 10^{-12} m^2 and the resulting convection in the aquifer results in a slight reduction of v_f and skews the distribution of total fault flow velocities toward slower values (**Figure 13**). Convection in the higher-permeability aquifer is also apparent in the distribution of total aquifer flow velocities. The distribution for $k_{aq} = 10^{-13}$ m^2 is bimodal, with the highest peak at low velocities, illustrating that flow velocities are negligible in the aquifer beyond the region immediately surrounding the fault zone. With $k_{aq} = 10^{-12}$ m^2, the velocity distribution is unimodal; there is convection throughout the entire aquifer (**Figure 13**). For all simulations, the distribution of v_f is unimodal.

The heat-flux fraction (HFF) is defined as the seafloor heat flux in the presence of fluid flow normalized by the background conductive heat flux value for that x-y location. HFF =1 indicates that there is no significant difference from

background in regional heat flux due to fluid flow. HFF patterns on x-direction transects perpendicular to fault strike over convective upwellings show a distinct peak associated with the fault trace (**Figure 14**).

When $k_{aq} = 10^{-13}$ m^2 and $k_f = 10^{-11}$ m^2, the median value of k_f for which v_f is significantly higher than v_{aq}, there is no systematic variation in the HFF peak height above a fault-zone upwelling with dip angle (**Figure 14a**). Peaks are roughly centered over the fault trace, and the minimum HFF peak height is ~1.9, a nearly twofold increase in regional seafloor heat flux associated with advection in the fault zone. In addition, there is a heat flux trough over the hanging wall (positive x-direction) for non-vertical faults, with suppression of 10-30% of background heat flux values. This trough widens and deepens with decreasing dip angle. For the 60° fault with $k_{aq} = 10^{-13}$ m^2, the $k_f = 10^{-13}$ m^2 peak is slightly skewed down dip relative to higher k_f peaks, perhaps because circulation in the aquifer is relatively significant compared to circulation in the fault, extracting heat before it can travel all the way to the fault trace (**Figure 14b**). For $k_f/k_{aq} > 1$, upwelling HFF peak heights are between 1.9 and 2.0. As illustrated in heat flux maps (**Figure 8, Figure 10**), relief between upwellings and downwellings decreases with increasing k_f. For the 60° fault with $k_{aq} = 10^{-12}$ m^2, signals from convection in the aquifer obscure the hanging wall HFF trough, but upwelling HFF peak heights for $k_f = 10^{-12}$ m^2 and $k_f = 10^{-11}$ m^2 still exceed 1.6, a significant and readily detectable local anomaly. The peaks at $k_{aq} = 10^{-12}$ m^2 are wider than those at $k_{aq} = 10^{-13}$ m^2, as circulation in the fault spreads into circulation in the aquifer.

3.3 Secondary simulation results: fault penetration depth

Circulation patterns and heat flux differ significantly when d_f is increased from 1 km to 3 km for $\theta = 60°$, $k_{aq} = 10^{-13}$ m^2, and $k_f = 10^{-12}$ m^2. Two differences are evident between the seafloor heat flux signals for $d_f = 1$ km and $d_f = 3$ km: the convection cells for $d_f = 3$ kmbsf are no longer all the same width at the fault trace, and the $d_f = 3$ kmbsf heat flux peak at the fault trace and trough down dip are wider and deviate more from background (**Figure 15**).

We investigate the first observation by visualizing the three-dimensional circulation pattern in the entire fault zone (**Figure 16**). The width of the convection cells varies with depth; this is the only simulation where upwellings and downwellings are not parallel to fault dip over the entire length of the fault. Overturn occurs only at the top and bottom of the fault zone. This pattern develops and persists as the simulation comes to dynamic steady state. We have no evidence of instability or oscillation in the convection pattern once heat output equals heat input. Following our earlier discussion, the threefold increase in d_f significantly increases in the amount of space in which convective fluid flow can occur, destabilizing the system and reducing the critical value of *Ra*. When $d_f = 3$ km, deeper, evenly spaced cells may be unstable and begin to collapse to the observed dynamic-steady-state configuration. $\hat{u}_d$ with $d_f = 3$ kmbsf is ~3 times greater than $\hat{u}_d$ with $d_f = 1$ kmbsf. Velocity metrics for total flow rates in the fault zone with $d_f = 3$ kmbsf do not differ significantly from those with $d_f = 1$ kmbsf (**Table 4**).

HFF transects support our second observation from the heat map; the peak and trough of the signal associated with both convective upwellings and downwellings for $d_f = 3$ kmbsf is much more pronounced (**Figure 17**). Upwelling peak height is HFF ~3.25, a threefold increase from background. Upwelling peak width is also greater; heat flux values are elevated by at least 50% of background (HFF = 1.5) up to 500 m beyond the fault trace in the positive and negative x-direction. The hanging wall HFF minimum is ~0.6. Heat flux is also depressed in the footwall (in the positive x-direction from fault trace). On both sides of the domain, heat flux values do not return

to background, indicating that the size of the domain may limit heat extraction by the fault in this simulation. Clearly, deeper faults are much more efficient at extracting crustal heat compared to shallower faults having properties that are otherwise similar.

3.4 Secondary simulation results: fault thickness

Unlike the t_f = 30 m result, there is no apparent characteristic convection wavelength in seafloor heat flux maps for t_f = 10 and 90 m (**Figure 18**). HFF peak height in a transect over a convective upwelling when t_f = 10 m is 2.6. HFF peak height in a transect over a convective upwelling when t_f = 90 m is 2.3 (**Figure 19**). The $\hat{u}_d$ and the value of v_f when t_f = 10 m are ~2 and ~3 times greater, respectively, than when t_f = 90 (**Table 5**). v_{aq} in the 10-m-thick fault is one order of magnitude smaller than in the 90-m-thick fault.

3.5 Secondary simulation results: aquifer thickness

Convection is more apparent in seafloor heat flux patterns with lower k_{aq} when t_{aq} = 600 m than when t_{aq} = 300 m; distinct cells form far from the fault zone when $k_{aq} = 10^{-13}$ m^2 (**Figure 20**). When k_{aq} is increased to 10^{-12} m^2, the relief of the heat flux variations associated with aquifer convection cells is reduced and the signals from individual upwellings widen and merge. Mean cell half-width (upwelling to downwelling distance) scales with aquifer thickness; when $k_{aq} = 10^{-12}$ m^2, cell half-width is 1 km when t_{aq} = 600 m, compared with 0.5 km when t_{aq} = 300 m. Convection in the thicker aquifer may destabilize the convection patterns observed at low k_{aq} in the thinner aquifer. Even when $k_{aq} = 10^{-13}$ m^2, convection in the fault zone consists of two upwellings and two downwellings at the same locations as those in the thinner

aquifer when $k_f = 10^{-11}$ m^2 and $k_{aq} = 10^{-13}$ m^2. It appears in this case that the fault convection signal has "broken down," as discussed in Section 3.2. Convection in the aquifer is apparent in transects for all values of k_{aq} when t_{aq} = 600 m (**Figure 21**). When t_{aq} = 600 m and $k_{aq} = 10^{-13}$ m^2 or 10^{-12} m^2, the HFF peak over the upwelling is ~2, similar to the result when t_{aq} = 300 m. When $k_{aq} = 10^{-12}$ m^2, the magnitude of the upwelling HFF signal from aquifer convection is reduced to 1.75 (still a significant signal). No hanging wall heat flux suppression is apparent with a thicker aquifer (no trough). Velocity metrics for t_{aq} = 600 m show trends similar to those in the t_{aq} = 300 m case; $\hat{u}_d$ and v_f increase with increasing k_f (**Table 6**).

We calculate *Ra* for the tabular aquifer (Equation 1), using average fluid and rock properties and assuming isothermal conditions at the top and bottom of the aquifer. For this geometry, convection occurs when *Ra* exceeds a critical value of 17.65 for isothermal upper and constant-heat-flux lower boundaries (Lapwood, 1948; Nield, 1968). In the 300-m-thick aquifer with $k_{aq} = 10^{-13}$ m^2, *Ra* is ~7 and there is no convection in the aquifer. When $k_{aq} = 10^{-12}$, *Ra* is ~44, consistent with observations of convection cells in the aquifer. In the 600-m-thick aquifer with $k_{aq} = 10^{-13}$ m^2, *Ra* is ~15, close to the critical value (about the same, given the approximate nature of *Ra* calculations for these systems). When $k_{aq} = 10^{-12}$, *Ra* is ~65, consistent with observations of convection cells in the aquifer.

4. Discussion

4.1 Dip angle: circulation patterns and heat extraction

One of the primary objectives of this study is to elucidate the interplay between increased flow rates in the fault zone due to thermal buoyancy in a vertical fault and more extensive mining of lithospheric heat by a fault with a shallower dip and larger horizontal projection. When $k_{aq} = 10^{-13}$ m^2 and $k_f \geq 10^{-12}$ m^2, i.e., when there is significant channeling of flow along the fault compared with circulation in the aquifer, median up-dip velocity ($\hat{u}_d$) peaks at intermediate values ($\theta = 45°$ or $60°$) (**Figure 11**). Interpreting $\hat{u}_d$ as a proxy for advection of fluid up fault zone, this indicates that there is an intermediate dip angle at which the dip-parallel flow rate is maximized. For all combinations of k_f and k_{aq} tested, the range of values of $\hat{u}_d$ narrows at $\theta = 90°$ compared to lower values of θ. This suggests that there is a shift at some near-vertical dip angle to convection driven predominantly by heating at the base of the fault, compared with convection in lower angle faults that is also driven by heat mined more widely over the longer horizontal projection of the shallow fault.

The seafloor heat flux signal associated with fault circulation differs with fault dip. For both $k_{aq} = 10^{-13}$ m^2 and 10^{-12} m^2, the heat flux trough located down dip from the fault trace is more pronounced at lower dip angles (**Figure 8**); heat flux is depressed to lower values over a wider lateral extent (**Figure 8, Figure 14a**). In our simulations, shallower faults have more total length in the aquifer than deeper faults, allowing for more extensive diversion of relatively warm fluid flow from the aquifer to the fault zone when $k_f > k_{aq}$. The height of the heat flux peak associated with upwelling on the fault zone does not vary significantly with dip angle, but there is a significant positive anomaly at the fault trace when $k_{aq} = 10^{-13}$ m^2 and $k_f \geq 10^{-12}$ m^2,

well above the 5% deviation from the regional background that might be reliably detected based on common uncertainties and errors in individual measurements (e.g., Hyndman et al., 1979; Wright and Louden, 1989; Fisher and Harris, 2010; **Figure 14**).

The HFF transects presented in this study, taken over a "characteristic" upwelling, are intended to represent the largest deviation from background and illustrate that an anomaly could be detected in field measurements. They are not a direct proxy for heat advected through the fault to the seafloor. Because the number of upwellings varies with θ, k_{aq}, and k_f, the single-upwelling HFF transect represents a fraction of total heat advected, the magnitude of which varies with number of upwellings, among other factors.

4.2 Fault-aquifer interactions

A permeability contrast between the fault and aquifer is required to develop a distinct heat flux anomaly along the fault trace. Convection in the aquifer results in additional heat flux anomalies that may hinder detection of the fault signal. That there is a strong positive correlation between permeability contrast and median velocity in the fault and no significant correlation between permeability contrast and median velocity in the aquifer (**Figure 11**) suggests that even vigorous convection in the fault has little effect on flow in more distant regions in the aquifer (except when $d_f = 3$ km, see Section 4.3). Obviously, this will depend in detail on the nature of connections between faults and crustal aquifers. That said, an aquifer with sufficiently high permeability relative to the fault may limit the focusing influence of the fault,

reducing the efficiency of the fault as a conduit for rising hot fluid and the magnitude and continuity of the heat flux signal above the fault trace.

4.3 Fault thickness and depth: circulation patterns and heat extraction

Median up-dip and total fault velocities are highest when t_f = 30 m, lower when t_f = 10 m, and lowest when t_f = 90 m (**Table 6**). Wider faults may not "channel" circulation as efficiently as narrower faults and tend to develop more diffuse convection cells. More diffuse convection in the wider fault may result in a temperature field that is more favorable for convection in the aquifer near the fault, which accounts for larger v_{aq} when t_f = 90 m compared with t_f = 10 m and 30 m. Taking median up-dip velocity as a proxy for heat advected to the seafloor through the fault, we would expect total heat flux at the fault trace to scale with both median up-dip velocity and fault width. To quantify heat flux associated with fluid circulation in the fault, we calculate a "positive heat flux anomaly" (H_f) for each simulation (**Table 7**). H_f is the sum of seafloor nodal heat flow values that exceed the conductive heat flow value by at least 1%, normalized by the area of the entire domain. H_f increases with t_f, despite the fact that up-dip velocity when t_f = 90 m is approximately one-sixth that when t_f = 30 m and one-half that when t_f = 10 m. That H_f does not increase linearly with up-dip velocity and fault width suggests that processes aside from up-dip advection, such as heat transfer between the fault and aquifer, also influence H_f.

We found that a fault that penetrates to 3 kmbsf extracts heat from a much larger region compared to a fault penetrating to 1 kmbsf. The deeper fault, with k_f =

10^{-12} m^2 and k_{aq} = 10-^{13} m^2, produces the largest upwelling heat flux signal of all simulations, HFF >3. The next largest non-edge upwelling signal is much lower, HFF ~ 2.. The deeper fault taps into hotter regions of the conductive basement. At these depths, the fault is the only part of the crust with properties that permit thermally significant fluid flow, and all advective heat extraction must occur within and at the edges of the fault zone. Compared with shallower faults, the deeper fault intercepts more heat from the conductive basement before it reaches the aquifer, resulting in more significant cooling of the hanging wall. Deeper faults may be more significant than shallow faults in influencing regional circulation patterns, even in the shallow upper crust.

4.4 Implications for field observations

Our simulations show that hydrothermal circulation in fault zones can produce heat flux anomalies in the sediment above the fault trace with magnitudes that exceed 100% of the background value, similar to the signals observed in surveys of ridge-flank regions where abyssal-hill-bounding normal faults are thought to guide fluid flow (e.g., Becker *et al.*, 1985; Hobart *et al*., 1985; Johnson *et al.*, 1993). Circulation patterns on ridge flanks are also guided by topography of the crustal aquifer (Fisher et al., 1990; Fisher and Becker, 1995; Davis et al., 1997; Hutnak et al., 2006). It may be difficult to isolate the heat flux signal due to fault-zone circulation from topography-driven circulation in the field and in more sophisticated models that incorporate basement topography, especially when faults and inflection points in basement topography are located close to each other (as in association with abyssal hills).

Our observation that circulation in a fault that taps the deep crust produces a large, wide thermal anomaly suggests that hydrothermal activity in a deep fault should be detectable at the seafloor in off-axis heat flow measurements. Such anomalies, however, are not present in global data sets (Stein, 2003; Hasterok, 2011). This suggests that deep penetration by faults that sustain hydrothermal activity from the shallow to deep crust or mantle may not be common. More specifically, our results indicate that the fluid circulation from the seafloor to the deep crust and upper mantle in faults on the outer rise of subducting slabs (e.g., Ranero *et al*., 2003) should produce a significant thermal anomaly; no such anomalies have been detected in surveys of subduction zones (Stein, 2003).

Simulations with deeper faults have more speculative implications for suggested circulation patterns and crustal structure on axis, in hydrothermal systems hosted by detachment faults. Faults that penetrate deep below the crustal aquifer can mine significant quantities of lithospheric heat and concentrate it in relatively small areas in the upper basement, which may be sufficient to drive systems such as the TAG hydrothermal field (Humphris *et al.*, 2015). DeMartin *et al*. (2007) suggested that fluid flow beneath the TAG hydrothermal field is focused in the detachment at depth but rises through the altered hanging wall closer to the seafloor. Our results indicate that circulation within a fault zone can depress temperatures within and seafloor heat flux above the hanging wall. Heterogeneity (e.g., increased permeability in the hanging wall or decreased permeability in the upper fault zone) and additional

high-transmissivity pathways in the hanging wall are necessary for heat advection to the shallow hanging wall.

In both oceanic and continental settings, faults zones are often characterized as "barrier-conduit" systems (e.g., Scibek *et al.*, 2016), in which the highly permeable fault zone core facilitates flow along the fault plane ("conduit") and the surrounding low-permeability damage zone (altered by melting, cataclasis, or fluid interaction) acts as a barrier to flow perpendicular to the fault plane (Caine *et al*., 1996). Our simulations do not include this complexity in fault structure, and rely entirely on the fault-aquifer permeability contrast to create conduit-like behavior. The presence of a damage zone, and heterogeneity in general, could allow for more focused flow along the fault zone in a high-permeability aquifer or in the presence of other circulation patterns, but may also limit the ability of the fault zone to extract heat by fluid advection from the surrounding crust.

Fluid circulation in fault zones is thought to be significant in other off-axis environments. Focused flow along faults in back-arc basins has been shown to fuel hydrothermal discharge and the formation of massive sulfide deposits (e.g., Schardt *et al*., 2006). Observations from mineralization ophiolites suggest that fluid circulation occurs in the deep crust (e.g., Zihlmann *et al*., 2017). Three-dimensional models that build on our study may be useful in evaluating the dynamics of these processes and determining whether heat flow signals could be used to confirm their activity.

The simulations presented in this study are first steps in a more comprehensive and nuanced analysis of fault zone hydrogeology in ridge-flank

oceanic crust. Future studies should continue to explore the topics addressed in simulations completed to date, as well as additional fault geometries (greater depths, listric profiles), more detailed fault zone structures (e.g., fault core, damaged country rock, variations in fault widths), the presence of multiple faults and their interactions, heterogeneous properties within both fault zones and host rock, variations in basement and seafloor relief, and the impacts of different sediment thicknesses, including regions where sediment cover is patchy or absent. As more simulations are developed, it will help to apply these to specific settings where some of the many free parameters are constrained by independent observations. Numerical simulation remains a valuable tool for understanding linked tectonic, geothermal, and hydrogeologic processes within ocean crust, but the large number of free parameters and unknown conditions makes it essential to integrate as much observational information as possible in assessing potential hydrologic scenarios.

5. Conclusions

We have presented the first three-dimensional, fully coupled simulations of heat and mass transport in fault zones in ridge-flank ocean crust. We simulated hydrothermal circulation over a range of fault and aquifer hydrologic properties for different fault geometries. We found that along-dip fluid flow in the fault zone is maximized at an intermediate dip angle (~45°), that a transition to primarily buoyancy-driven vertical flow occurs near 90°, and that circulation in faults that penetrate deeper into basement produces a more prominent heat flux anomaly at the fault trace and can significantly depress heat flux in the surrounding region. Seafloor

heat flux signals from convection in the crustal aquifer may obscure the signal from circulation in a fault; the signals associated with fault zone convection are likely coupled with those associated with basement topography and other local heterogeneities in the field.

This study provides the foundation for future, more complex simulations of hydrothermal circulation facilitated by fault zones in ocean crust. The numerical meshes used in this study can be used to further explore a broader range of hydrologic properties and to design additional meshes for studies with different system geometry. Future simulations should also explore the effect of heterogeneous permeability distributions and irregular lithologic boundaries in the upper crust, as well as more complex fault and damage zone structures. Incorporation of transient behaviors such as changes in permeability with exposure to hydrothermal fluids and investigation of the effects of initial conditions on stable circulation pattern development will help better characterize fluid flow and heat extraction at these sites.

Acknowledgements

We thank C.W. Gable and P.H. Stauffer for their significant assistance in designing the numerical mesh and running simulations. This research was supported by National Science Foundation grants OIA- 0939564, OCE-1260408, OCE-1355870 and Department of Energy grant DE-FE0029219 to LDEO (subaward GG013105 to UCSC). This is C-DEBI contribution 394.

References

Alt, J.C., 2004. Alteration of the upper oceanic crust: mineralogy, chemistry, and

processes, in: Davis, E.E., Elderfield, H. (Eds.), Hydrogeology of the Oceanic Lithosphere. Cambridge University Press, Cambridge, UK, 456–488.

Alt, J.C., Shanks, W.C., Bach, W., Paulick, H., Garrido, C.J., Beaudoin, G., 2007. Hydrothermal alteration and microbial sulfate reduction in peridotite and gabbro exposed by detachment faulting at the Mid-Atlantic Ridge, 15°20′N (ODP Leg 209): A sulfur and oxygen isotope study. Geochem. Geophys. Geosyst. 8, Q08002. doi: 10.1029/2007GC001617

Amend, J.P., Teske, A., 2005. Expanding frontiers in deep subsurface microbiology. Palaeogeogr. Palaeoclimatol, Palaeoecol. 219, 131–155. doi:10.1016/j.palaeo.2004.10.018

Andersen, C., Rüpke, L., Hasenclever, J., Petersen, S., 2015. Fault geometry and permeability contrast control vent temperatures at the Logatchev 1 hydrothermal field, Mid-Atlantic Ridge. Geology 43, 51–54. doi: 10.1130/G36113.1

Bach, W., Banerjee, N.R., Dick, H.J.B., Baker, E.T., 2002. Discovery of ancient and active hydrothermal systems along the ultra-slow spreading Southwest Indian Ridge 10°–16°E. Geochem. Geophys. Geosyst. 3, 1–14. doi:10.1029/2001GC000279

Bach, W., Peucker-Ehrenbrink, B., Hart, S.R., Blusztajn, J.S., 2003. Geochemistry of hydrothermally altered oceanic crust: DSDP/ODP Hole 504B - Implications for seawater-crust exchange budgets and Sr- and Pb-isotopic evolution of the mantle. Geochem. Geophys. Geosyst. 4, 8904. doi:10.1029/2002GC000419

Baker, E.T., Edmonds, H.N., Michael, P.J., Bach, W., Dick, H.J.B., Snow, J.E., Walker, S.L., Banerjee, N.R., Langmuir, C.H., 2004. Hydrothermal venting in magma deserts: The ultraslow-spreading Gakkel and Southwest Indian Ridges. Geochem. Geophys. Geosyst. 5, Q08002. doi:10.1029/2004GC000712

Baker, P.A., Stout, P.M., Kastner, M., Elderfield, H., 1991. Large-scale lateral advection of seawater through oceanic crust in the central equatorial Pacific. Earth Planet. Sci. Lett. 105, 522–533. doi:10.1016/0012-821X(91)90189-O

Barker, A.K., Coogan, L.A., Gillis, K.M., Hayman, N.W., Weis, D., 2010. Direct observation of a fossil high-temperature, fault-hosted, hydrothermal upflow zone in crust formed at the East Pacific Rise. Geology 38, 379–382. doi:https://doi.org/10.1130/G30542.1

Becker, K., Fisher, A.T., Tsuji, T., 2013. New packer experiments and borehole logs in upper oceanic crust: Evidence for ridge-parallel consistency in crustal hydrogeological properties: Basaltic Crust Hydrological Continuity. Geochem. Geophys. Geosyst. 14, 2900–2915. doi:10.1002/ggge.20201

Becker, K., Langseth, M.G., Von Herzen, R.P., Anderson, R.N., Hobart, M.A., 1985. Deep crustal geothermal measurements, Hole 504B, Deep Sea Drilling Project Legs 69, 70, 83 and 92 in: Anderson, R.N. (Ed.), Initial Reports DSDP, Leg 83, Balboa to Balboa, Panama. US Govt. Printing Office; UK distributors, IPOD Committee, NERC, Swindon, 405–418.

Becker, K., Morin, R.H., Davis, E.E., 1994. Permeabilities in the Middle Valley

hydrothermal system measured with packer and flowmeter experiments. Proceedings of the Ocean Drilling Program, Scientific Results 139, 613-626.

Benjamin, S.B., Haymon, R.M., 2006. Hydrothermal mineral deposits and fossil biota from a young (0.1 Ma) abyssal hill on the flank of the fast spreading East Pacific Rise: Evidence for pulsed hydrothermal flow and tectonic tapping of axial heat and fluids. Geochem. Geophys. Geosyst. 7, Q05002. doi:10.1029/2005GC001011

Boschi, C., Früh-Green, G.L., Delacour, A., Karson, J.A., Kelley, D.S., 2006. Mass transfer and fluid flow during detachment faulting and development of an oceanic core complex, Atlantis Massif (MAR 30 °N). Geochem. Geophys. Geosyst. 7, Q01004. doi:10.1029/2005GC001074

Caine, J.S., Evans, J.P., Forster, C.B., 1996. Fault zone architecture and permeability structure. Geology 24, 1025-1028. doi:10.1130/0091-7613(1996)024<1025:FZAAPS>2.3.CO;2

Canales, J.P., Sohn, R.A., deMartin, B.J., 2007. Crustal structure of the Trans-Atlantic Geotraverse (TAG) segment (Mid-Atlantic Ridge, 26°10′N): Implications for the nature of hydrothermal circulation and detachment faulting at slow spreading ridges. Geochem. Geophys. Geosyst. 8, Q08004. doi:10.1029/2007GC001629

Cannat, M., Sauter, D., Mendel, V., Ruellan, E., Okino, K., Escartin, J., Combier, V., Baala, M., 2006. Modes of seafloor generation at a melt-poor ultraslow-spreading ridge. Geology 34, 605. doi:10.1130/G22486.1

Cheadle, M., Grimes, C., 2010. Structural geology: To fault or not to fault. Nature Geosci. 3, 454–456. doi:10.1038/ngeo910

Cherubini, Y., Cacace, M., Blöcher, G., Scheck-Wenderoth, M., 2013a. Impact of single inclined faults on the fluid flow and heat transport: results from 3-D finite element simulations. Environ. Earth Sci. 70, 3603–3618. doi:10.1007/s12665-012-2212-z

Cherubini, Y., Cacace, M., Scheck-Wenderoth, M., Moeck, I., Lewerenz, B., 2013b. Controls on the deep thermal field: implications from 3-D numerical simulations for the geothermal research site Groß Schönebeck. Environ. Earth Sci. 70, 3619–3642. doi:10.1007/s12665-013-2519-4

Cherubini, Y., Cacace, M., Scheck-Wenderoth, M., Noack, V., 2014. Influence of major fault zones on 3-D coupled fluid and heat transport for the Brandenburg region (NE German Basin). Geothermal Energy Sci. 2, 1–20. doi:10.5194/gtes-2-1-2014

Coogan, L.A., Howard, K.A., Gillis, K.M., Bickle, M.J., Chapman, H., Boyce, A.J., Jenkin, G.R.T., Wilson, R.N., 2006. Chemical and thermal constraints on focussed fluid flow in the lower oceanic crust. Am. J. Sci. 306, 389–427. doi:10.2475/06.2006.01

Davis, E.E., Chapman, D.S., Forster, C.B., Villinger, H., 1989. Heat-flow variations correlated with buried basement topography on the Juan de Fuca Ridge flank. Nature 342, 533–537. doi:10.1038/342533a0

Davis, E.E., Chapman, D.S., Mottl, M.J., Bentkowski, W.J., Dadey, K., Forster, C.,

Harris, R., Nagihara, S., Rohr, K., Wheat, G., Whiticar, M., 1992. FlankFlux: an experiment to study the nature of hydrothermal circulation in young oceanic crust. Can. J. Earth Sci. 29, 925–952. doi:10.1139/e92-078

Davis, E. E., K. Wang, J. He, D. S. Chapman, H. Villinger, and A. Rosenberger (1997), An unequivocal case for high Nusselt-number hydrothermal convection in sediment-buried igneous oceanic crust, *Earth Planet. Sci. Lett. 146*, 137-150.

Delaney, J.R., Robigou, V., McDuff, R.E., Tivey, M.K., 1992. Geology of a vigorous hydrothermal system on the Endeavor segment, Juan de Fuca Ridge. J. Geophys. Res. 97, 19663–19682.

deMartin, B.J., Sohn, R.A., Canales, J.P., Humphris, S.E., 2007. Kinematics and geometry of active detachment faulting beneath the Trans-Atlantic Geotraverse (TAG) hydrothermal field on the Mid-Atlantic Ridge. Geology 35, 711–714.

Dilek, Y., 1998. Structure and teconics of intermediate-spread oceanic crust drilled at DSDP/ODP Holes 504B and 896A, Costa Rica Rift, in: Cramp, A., MacLeod, C.J., Lee, S.V., Jones, E.J.W. (Eds.), Geological Evolution of Oceanic Basins: Results from the Ocean Drilling Program. Geological Society, London, Special Publications, 179–197.

Edwards, K.J., Bach, W., McCollom, T.M., 2005. Geomicrobiology in oceanography: microbe–mineral interactions at and below the seafloor. Trends in Microbiology 13, 449–456. doi:10.1016/j.tim.2005.07.005

Ehrhardt, C.J., Haymon, R.M., Lamontagne, M.G., Holden, P.A., 2007. Evidence for hydrothermal Archaea within the basaltic flanks of the East Pacific Rise. Environ. Microbio. 9, 900–912. doi:10.1111/j.1462-2920.2006.01211.x

Elderfield, H., Schultz, A., 1996. Mid-ocean ridge hydrothermal fluxes and the chemical composition of the ocean. Annu. Rev. Earth Planet. Sci. 24, 191–224.

Escartín, J., Mével, C., MacLeod, C.J., McCaig, A.M., 2003. Constraints on deformation conditions and the origin of oceanic detachments: The Mid-Atlantic Ridge core complex at 15°45′N. Geochem. Geophys. Geosyst. 4, 1067. doi:10.1029/2002GC000472

Faccenda, M., Gerya, T.V., Burlini, L., 2009. Deep slab hydration induced by bending-related variations in tectonic pressure. Nature Geosci. 2, 790–793. doi:10.1038/ngeo656

Fairley, J.P., 2009. Modeling fluid flow in a heterogeneous, fault-controlled hydrothermal system. Geofluids 9, 153–166. doi:10.1111/j.1468-8123.2008.00236.x

Fisher, A.T., Alt, J., Bach, W., 2014. Hydrogeologic Properties, Processes, and Alteration in the Igneous Ocean Crust, in: Developments in Marine Geology. Elsevier, 507–551. doi:10.1016/B978-0-444-62617-2.00018-9

Fisher, A.T., Becker, K., 2000. Channelized fluid flow in oceanic crust reconciles heat-flow and permeability data. Nature 403, 71–74.

Fisher, A.T., Becker, K., 1995. Correlation between seafloor heat flow and basement

relief: Observational and numerical examples and implications for upper crustal permeability. J. Geophys. Res. 100, 12641–12657. doi:10.1029/95JB00315

Fisher, A.T., Davis, E.E., Becker, K., 2008. Borehole-to-borehole hydrologic response across 2.4 km in the upper oceanic crust: Implications for crustal-scale properties. J. Geophys. Res. 113, B07106. doi:10.1029/2007JB005447

Fisher, A.T., Harris, R.N., 2010. Using seafloor heat flow as a tracer to map subseafloor fluid flow in the ocean crust. Geofluids 10, 142–160. doi:10.1111/j.1468-8123.2009.00274.x

Fisher, A.T., Wheat, C.G., 2010. Seamounts as conduits for massive fluid, heat, and solute fluxes on ridge flanks. Oceanography 23, 74–87.

Geist, E.L., 1999. Local tsunamis and earthquake source parameters. Advances in Geophysics 39, 117-209.

George, D., 1997. Unstructured 3D grid toolbox for modeling and simulation, LA-UR-97-3052, Los Alamos Grid Toolbox (LaGriT), available at lagrit.lanl.gov.

Giambalvo, E.R., Fisher, A.T., Martin, J.T., Darty, L., Lowell, R.P., 2000. Origin of elevated sediment permeability in a hydrothermal seepage zone, eastern flank of the Juan de Fuca Ridge, and implications for transport of fluid and heat. J. Geophys. Res. 105, 913–928. doi:10.1029/1999JB900360

Harris, M., Coggon, R.M., Wood, M., Smith-Duque, C.E., Henstock, T.J., Teagle, D.A.H., 2017. Hydrothermal cooling of the ocean crust: Insights from ODP Hole 1256D. Earth and Planet. Sci. Lett. 462, 110–121.

doi:10.1016/j.epsl.2017.01.010

Hart, R., Hoefs, J., Pyle, D., 1990. Multistage Hydrothermal Systems in the Blanco Fracture Zone, in: McMurray, G.R. (Ed.), Gorda Ridge: A Seafloor Spreading Center in the United States' Exclusive Economic Zone. Springer New York, New York, NY, pp. 51–75. doi:10.1007/978-1-4612-3258-2_4

Harvey, A.H., Peskin, A.P., Klein, S.A., 1997. NIST/ASME Steam Properties, NIST Standard Reference Database 10, Version 2.1. Standard Reference Data Program, NIST, Gaithersburg, MD.

Hasterok, D., 2013. A heat flow based cooling model for tectonic plates. Earth and Planet. Sci. Lett. 361, 34–43. doi:10.1016/j.epsl.2012.10.036

Hasterok, D., Chapman, D.S., Davis, E.E., 2011. Oceanic heat flow: Implications for global heat loss. Earth and Planet. Sci. Lett. 311, 386–395. doi:10.1016/j.epsl.2011.09.044

Hayman, N.W., Karson, J.A., 2009. Crustal fluids exposed in the Pito Deep Rift: Conduits for hydrothermal fluids on the southeast Pacific Rise. Geochem. Geophys. Geosyst. 10, Q02013. doi:10.1029/2008GC002319

Hayman, N.W., Karson, J.A., 2007. Faults and damage zones in fast-spread crust exposed on the north wall of the Hess Deep Rift: Conduits and seals in seafloor hydrothermal systems. Geochem. Geophys. Geosyst. 8, Q10002. doi:10.1029/2007GC001623

Haymon, R.M., Koski, R.A., Abrams, M.J., 1989. Hydrothermal discharge zones beneath massive sulfide deposits mapped in the Oman ophiolite. Geology 17,

531–535. doi:https://doi.org/10.1130/0091-7613(1989)017<0531:HDZBMS>2.3.CO;2

Haymon, R.M., Macdonald, K.C., Benjamin, S.B., Ehrhardt, C.J., 2005. Manifestations of hydrothermal discharge from young abyssal hills on the fast-spreading East Pacific Rise flank. Geology 33, 153–156. doi:10.1130/G21058.1

Hekinian, R., 2014. Fracture Zones and Transform Faults, in: Hekinian, R. (Ed.), Sea Floor Exploration: Scientific Adventures Diving into the Abyss. Springer International Publishing, Cham, 255–300. doi:10.1007/978-3-319-03203-0_8

Hobart, M.A., Langseth, M.G., Anderson, R.N., 1985. A geothermal and geophysical survey on the south flank of the Costa Rica Rift: Sites 504 and 505. Initial Reports of the Deep Sea Drilling Program 83, 379–404.

Humphris, S.E., Tivey, M.K., Tivey, M.A., 2015. The Trans-Atlantic Geotraverse hydrothermal field: A hydrothermal system on an active detachment fault. Deep Sea Research Part II: Topical Studies in Oceanography 121, 8–16. doi:10.1016/j.dsr2.2015.02.015

Hutnak, M., Fisher, A.T., Zühlsdorff, L., Spiess, V., Stauffer, P.H., Gable, C.W., 2006. Hydrothermal recharge and discharge guided by basement outcrops on 0.7-3.6 Ma seafloor east of the Juan de Fuca Ridge: Observations and numerical models. Geochem. Geophys. Geosyst. 7, Q07O02. doi:10.1029/2006GC001242

Hyndman, R.D., Davis, E.E., Wright, J.A., 1979. The measurement of marine

geothermal heat flow by a multipenetration probe with digital acoustic telemetry and insitu thermal conductivity. Marine Geophysical Researches 4, 181–205. doi:10.1007/BF00286404

Ingebritsen, S., Geiger, S., Hurwitz, S., Driesner, T., 2010. Numerical simulation of magmatic hydrothermal systems. Rev. Geophys. 48, RG1002. doi:10.1029/2009RG000287

Johnson, H.P., Becker, K., Von Herzen, R., 1993. Near-axis heat flow measurements on the northern Juan de Fuca ridge: Implications for fluid circulation in oceanic crust. Geophys. Res. Lett. 20, 1875–1878.

Ju, M., Yang, J., 2011. Numerical modeling of coupled fluid flow, heat transport and mechanical deformation: An example from the Chanziping ore district, South China. Geoscience Frontiers 2, 577–582. doi:10.1016/j.gsf.2011.07.005

Kappel, E. S., and W. B. F. Ryan (1986), Volcanic episodicity and a non-steady state rift valley along the northeast pacific spreading centers: evidence from Sea MARC I, J. Geophys. Res. 91(B14), 13925-13940. doi:10.1029/JB091iB14p13925.

Karson, J.A., Tivey, M.A., Delaney, J.R., 2002. Internal structure of uppermost oceanic crust along the Western Blanco Transform Scarp: Implications for subaxial accretion and deformation at the Juan de Fuca Ridge. J. Geophys. Res. 107, 2818. doi:10.1029/2000JB000051

Lapwood, E.R., 1948. Convection of a fluid in a porous medium. Mathematical Proceedings of the Cambridge Philosophical Society 44, 508. doi:10.1017/S030500410002452X

Lopez, D.L., Smith, L., 1996. Fluid flow in fault zones: Influence of hydraulic anisotropy and heterogeneity on the fluid flow and heat transfer regime. Water Resour. Res. 32, 3227–3235.

Lopez, D.L., Smith, L., 1995. Fluid flow in fault zones: Analysis of the interplay of convective circulation and topographically driven groundwater flow. Water Resour. Res. 31, 1489–1503.

Ludwig, W.J., Ewing, J.I., Ewing, S., Murachi, N., Den, N., Asano, S., Hotta, H., Hayakawa, M., Asanuma, T., Ichikawa, K., Noguchi, I., 1966. Sediments and structure of the Japan Trench. J. Geophys. Res. 71, 2121–2137. doi:10.1029/JZ071i008p02121

Macdonald, K.C., Fox, P.J., Alexander, R.T., Pockalny, R., Gente, P., 1996. Volcanic growth faults and the origin of Pacific abyssal hills. Nature 380, 125–129. doi:10.1038/380125a0

Macdonald, K.C., Luyendyk, B.P., 1985. Investigation of faulting and abyssal hill formation on the flanks of the East Pacific Rise (21°N) using ALVIN. Marine Geophysical Researches 7, 515–535. doi:10.1007/BF00368953

McCaig, A.M., Cliff, R.A., Escartin, J., Fallick, A.E., MacLeod, C.J., 2007. Oceanic detachment faults focus very large volumes of black smoker fluids. Geology 35, 935–938.

Mottl, M.J., Wheat, G., Baker, E., Becker, N., Davis, E., Feely, R., Grehan, A., Kadko, D., Lilley, M., Massoth, G., others, 1998. Warm springs discovered on 3.5 Ma oceanic crust, eastern flank of the Juan de Fuca Ridge. Geology 26,

51–54.

Naliboff, J.B., Billen, M.I., Gerya, T., Saunders, J., 2013. Dynamics of outer-rise faulting in oceanic-continental subduction systems. Geochem. Geophys. Geosyst. 14, 2310–2327. doi:10.1002/ggge.20155

Neira, N.M., Clark, J.F., Fisher, A.T., Wheat, C.G., Haymon, R.M., Becker, K., 2016. Cross-hole tracer experiment reveals rapid fluid flow and low effective porosity in the upper oceanic crust. Earth Planet. Sci. Lett. 450, 355–365. doi:10.1016/j.epsl.2016.06.048

Nield, D.A., 1968. Onset of thermohaline convection in a porous medium. Water Resour. Res. 4, 553–560.

Peacock, S.M., 2001. Are the lower planes of double seismic zones caused by serpentine dehydration in subducting oceanic mantle? Geology 29, 299–302. doi:10.1130/0091-7613(2001)029<0299:ATLPOD>2.0.CO;2

Pearson, M., Hofstra, A., Sweetkind, D., Stone, W., Cohen, D., Gable, C.W., Banerjee, A., 2012. Analytical and numerical models of hydrothermal fluid flow at fault intersections: Fluid flow at fault intersections. Geofluids 12, 312–326. doi:10.1111/gfl.12002

Ranero, C.R., Morgan, J.P., McIntosh, K., Reichert, C., 2003. Bending-related faulting and mantle serpentinization at the Middle America trench. Nature 425, 367.

Ranero, C.R., Villasenor, A., Phipps Morgan, J., Weinrebe, W., 2005. Relationship between bend-faulting at trenches and intermediate-depth seismicity.

Geochem. Geophys. Geosyst. 6, Q12002. doi:10.1029/2005GC000997

Rona, P.A., Widenfalk, L., Boström, K., 1987. Serpentinized ultramafics and hydrothermal activity at the Mid-Atlantic Ridge crest near 15°N. J. Geophys. Res. 92, 1417–1427. doi:10.1029/JB092iB02p01417

Rosenberg, N., A. T. Fisher, and J. Stein (2000), Large-scale lateral heat and fluid transport in the seafloor: revisiting the well-mixed aquifer model, Earth Planet. Sci. Lett., 182, 93-101. doi:10.1016/S0012-821X(00)00235-1

Saccocia, P.J., Gillis, K.M., 1995. Hydrothermal upflow zones in the oceanic crust. Earth Planet. Sci. Lett. 136, 1–16. doi:10.1016/0012-821X(95)00155-5

Salisbury, M.H., Keen, C.E., 1993. Listric faults imaged in oceanic crust. Geology 21, 117–120.

Schardt, C., Large, R., Yang, J., 2006. Controls on heat flow, fluid migration, and massive sulfide formation of an off-axis hydrothermal system—the Lau basin perspective. American Journal of Science 306, 103–134. doi: 10.2475/ajs.306.2.103

Scibek, J., Gleeson, T., McKenzie, J.M., 2016. The biases and trends in fault zone hydrogeology conceptual models: global compilation and categorical data analysis. Geofluids 16, 782–798. doi:10.1111/gfl.12188

Smith, D.K., Cann, J.R., Escartín, J., 2006. Widespread active detachment faulting and core complex formation near 13° N on the Mid-Atlantic Ridge. Nature 442, 440–443. doi:10.1038/nature04950

Spinelli, G.A., Giambalvo, E.R., Fisher, A.T., 2004. Sediment permeability,

distribution, and influence on fluxes in oceanic basement. Hydrogeology of the oceanic lithosphere 1, 151.

Stein, C.A., Stein, S., 1994. Constraints on hydrothermal flux through the oceanic lithosphere from global heat flow. J. Geophys. Res. 99, 3081–3095.

Stein, C.A., Stein, S., 1992. A model for the global variation in oceanic depth and heat flow with lithospheric age. Nature 359, 123–129.

Stein, Carol A., 2003, Heat Flow and Flexure at Subduction Zones. Geophys. Res. Lett. 30(23), 2197. doi:10.1029/2003GL018478

Stein, J. S., and A. T. Fisher (2003), Observations and models of lateral hydrothermal circulation on a young ridge flank: numerical evaluation of thermal and chemical constraints, Geochem. Geophys. Geosyst. 4(3), 1026 doi: 10.1029/2002GC000415

Tivey, M.A., Schouten, H., Kleinrock, M.C., 2003. A near-bottom magnetic survey of the Mid-Atlantic Ridge axis at 26°N: Implications for the tectonic evolution of the TAG segment. J. Geophys. Res. 108(B5), 2277. doi:10.1029/2002JB001967

Varnavas, S.P., 1988. Hydrothermal metallogenesis at the Wilkes Fracture Zone — East Pacific Rise intersection. Marine Geology 79, 77–103. doi:10.1016/0025-3227(88)90158-2

Villinger, H., Grevemeyer, I., Kaul, N., Hauschild, J., Pfender, M., 2002. Hydrothermal heat flux through aged oceanic crust: where does the heat escape? Earth Planet. Sci. Lett. 202, 159–170. doi:10.1016/S0012-821X(02)00759-8

Wang, K., He, J., Davis, E.E., 1997. Influence of basement topography on hydrothermal circulation in sediment-buried igneous oceanic crust. Earth Planet. Sci. Lett.146, 151–164.

Wheat, C.G., Elderfield, H., Mottl, M.J., Monnin, C., 2000. Chemical composition of basement fluids within an oceanic ridge flank: Implications for along-strike and across-strike hydrothermal circulation. J. Geophys. Res. 105, 13437–13447. doi:10.1029/2000JB900070

Wheat, C.G., Mottl, M.J., 2004. Geochemical fluxes through mid-ocean ridge flanks, in: Davis, E.E., Elderfield, H. (Eds.), Hydrogeology of the Oceanic Lithosphere. Cambridge University Press, Cambridge, UK, 627–658.

Williams, D.L., Green, K., van Andel, T.H., Von Herzen, R.P., Dymond, J.R., Crane, K., 1979. The hydrothermal mounds of the Galapagos Rift: Observations with DSRV Alvin and detailed heat flow studies. J. Geophys. Res. 84, 7464–7484. doi:10.1029/JB084iB13p07467

Winslow, D.M., Fisher, A.T., 2015. Sustainability and dynamics of outcrop-to-outcrop hydrothermal circulation. Nature Communications 6, 7567. doi:10.1038/ncomms8567

Winslow, D.M., Fisher, A.T., Stauffer, P.H., Gable, C.W., Zyvoloski, G.A., 2016. Three-dimensional modeling of outcrop-to-outcrop hydrothermal circulation on the eastern flank of the Juan de Fuca Ridge: Three-Dimensional Ridge-Flank Hydrothermal Modeling. J. Geophys. Res. 121, 1365–1382. doi:10.1002/2015JB012606

Wright, J.A. and Louden, K.E., 1989, CRC handbook of seafloor heat flow. CRC series in marine science, CRC Press, Boca Raton, Fla.

Wolery, T.J., Sleep, N.H., 1976. Hydrothermal circulation and geochemical flux at mid-ocean ridges. J. Geology 84, 249–275.

Yang, J., 2002. Influence of normal faults and basement topography on ridge-flank hydrothermal fluid circulation. Geophysical Journal International 151, 83–87.

Yang, J., 1996. Fracture-induced hydrothermal convection in the oceanic crust and the interpretation of heat-flow data. Geophys. Res. Lett. 23, 929–932.

Zhao, C., Hobbs, B., Ord, A., 2009. Convective and Advective Heat Transfer in Geological Systems. J. Geochem. Explor. 101, 128 doi:10.1016/j.gexplo.2008.11.002

Zhao, C., Hobbs, B.E., Ord, A., Kühn, M., Mühlhaus, H.B., Peng, S., 2006. Numerical simulation of double-diffusion driven convective flow and rock alteration in three-dimensional fluid-saturated geological fault zones. Computer Methods in Applied Mechanics and Engineering 195, 2816–2840. doi:10.1016/j.cma.2005.07.008

Zihlmann, B., Müller, S., Koepke, J., Teagle, D., 2017. Hydrothermal fault zones in the lower oceanic crust: An example from the Samail ophiolite, Oman. EGU General Assembly Conference Abstracts, 19, 6552.

Zyvoloski, G.A., Robinson, B.A., Dash, Z.V., Kelkar, S., Viswanathan, H.S., Pawar, R.J., Stauffer, P.H., 2011. Software users manual (UM) for the FEHM application version 3.1-3.X.

Figure 1. Cross-sectional schematics of fault types. A. Detachment faults (modified from deMartin *et al*. (2007)); B. Subduction zone outer-rise fault (modified from Geist (1999)); C. Abyssal hill normal and volcanic growth faults (modified from MacDonald *et al*. (1996)); D. Transform faults and fracture zones).

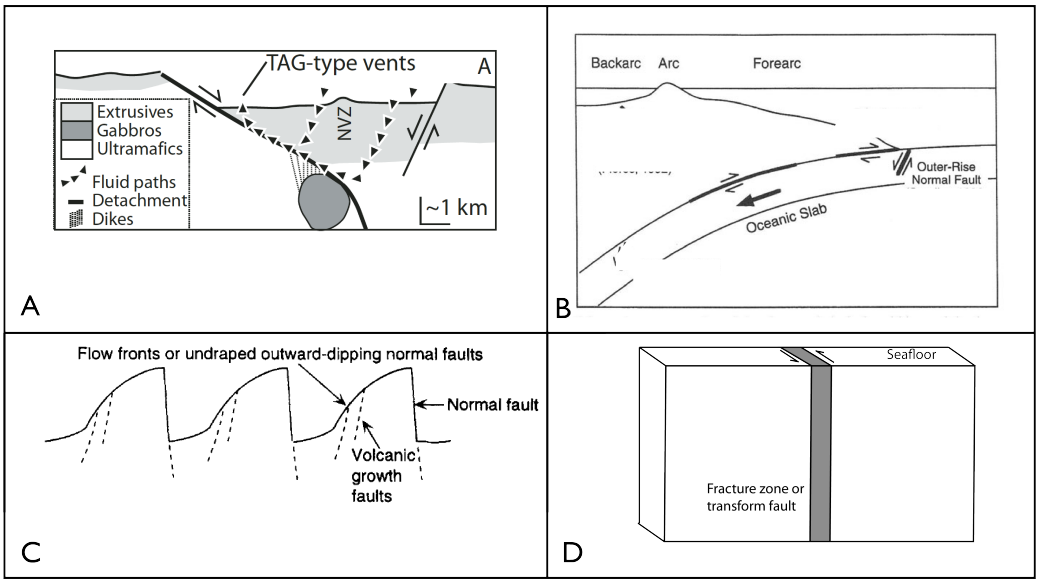

Figure 2. Schematic of hypotheses. How do the geometry and properties of a fault in ocean crust affect circulation and seafloor heat flux patterns? $Q_{\text{lithospheric}}$ and Q_{fault} are basal lithospheric heat flux input and seafloor heat flux output, respectively. h_f is the length of the horizontal projection of the fault plane, which decreases with increasing dip angle.

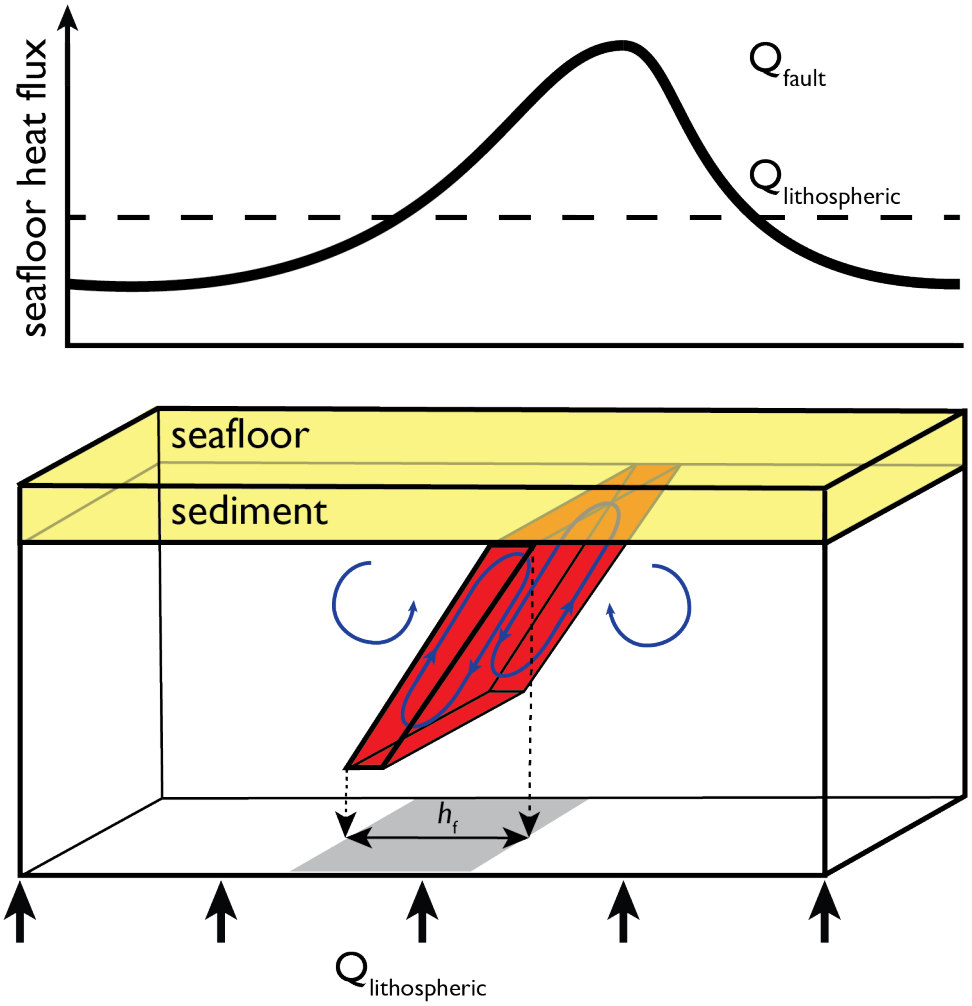

Figure 3. a. Mesh schematic, not to scale. Yellow region is marine sediment, blue the crustal aquifer, green the conductive basement, and red the fault zone. k_s, k_{aq}, k_f, and k_c are the permeabilities of the sediment, aquifer, fault, and conductive basement, respectively. t_s, t_{aq}, and t_f are the thicknesses of the sediment, aquifer, fault, and conductive basement, respectively. d_f is depth into basement into which fault penetrates. θ is fault dip angle. The width of the entire domain is ~4 times larger than d_f. **b.** Boundary conditions. Top of the domain is held at bottom-water temperature of 2 °C and hydrostatic pressure. Bottom of domain is subject to constant heat flux of 180 mW/m^2 and is closed to fluid flow. Sides are no-flow boundaries for both heat and fluid.

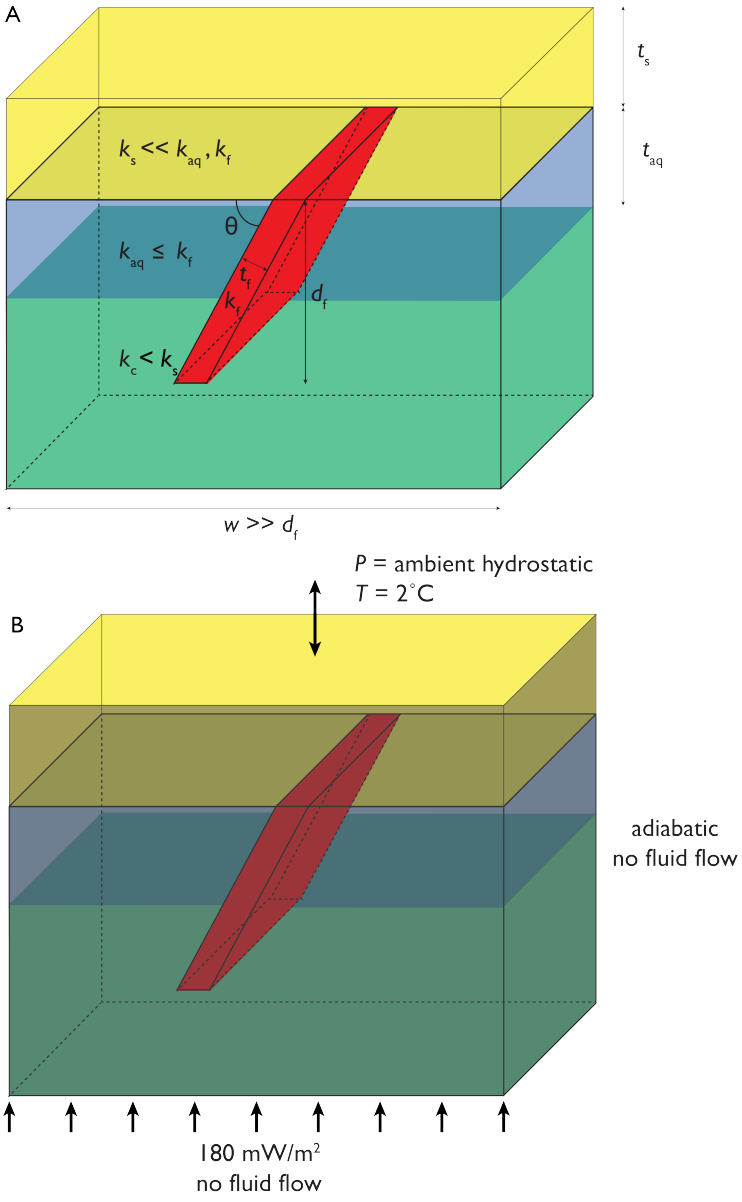

Figure 4. a. The high-resolution zone of the numerical mesh surrounding the fault zone, the region outlined by the white box in the complete mesh, shown in **b.** Yellow region is marine sediment, blue the crustal aquifer, green the conductive basement, and red the fault zone.

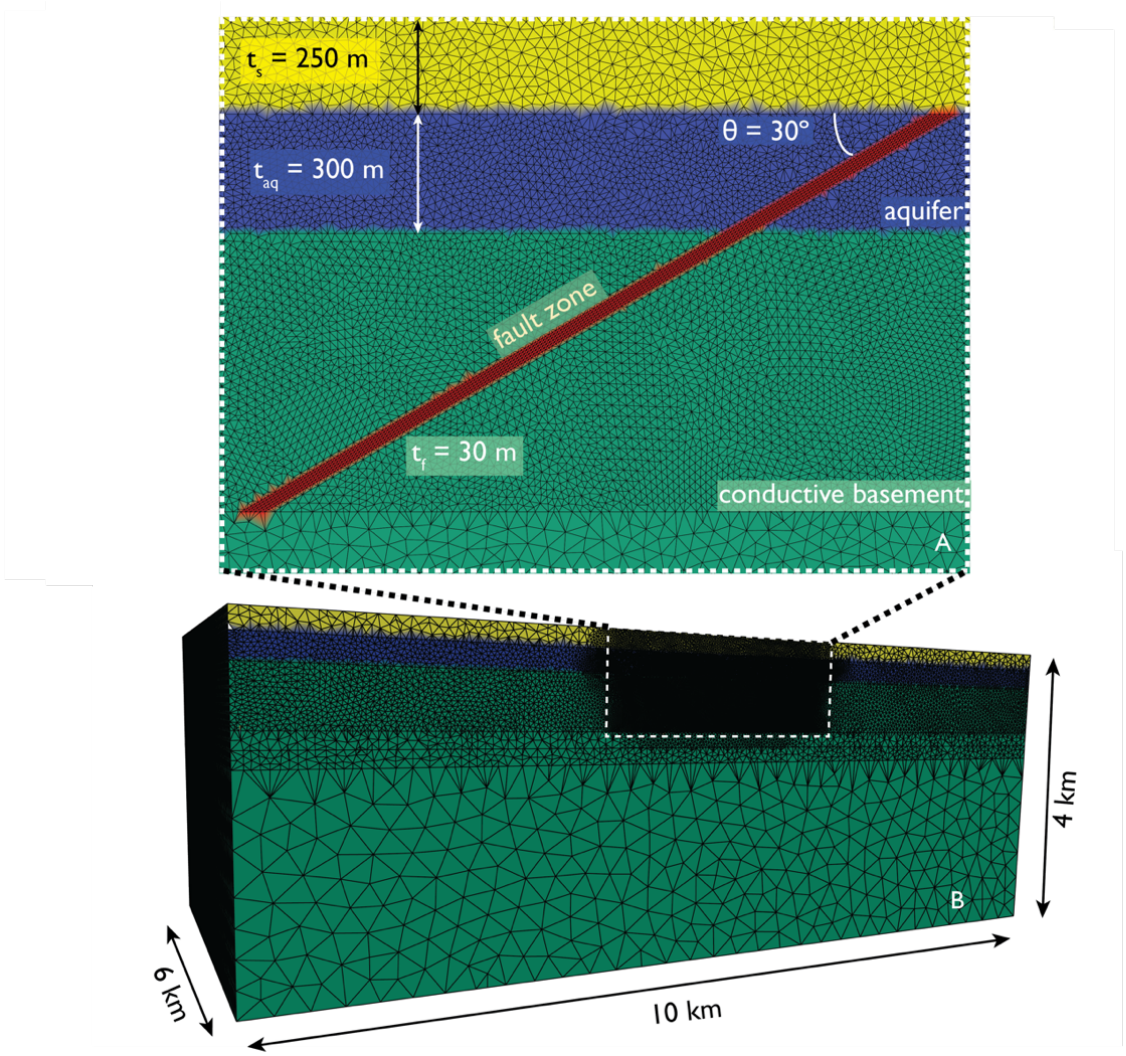

Figure 5. a. Simulation output showing the temperature field at dynamic steady state for a 60° fault with $k_{aq} = 10^{-13}$ m^2 and $k_f = 10^{-11}$. The conductive profile is warped at the fault tips, with temperature lowered at the terminus of the fault in the conductive basement and elevated at the top of the fault at the sediment-basement interface. **b.** Three-dimensional patterns of hydrothermal circulation. Flow vectors are plotted on a natural-log scale. The hanging wall has been removed to make flow vectors more visible.

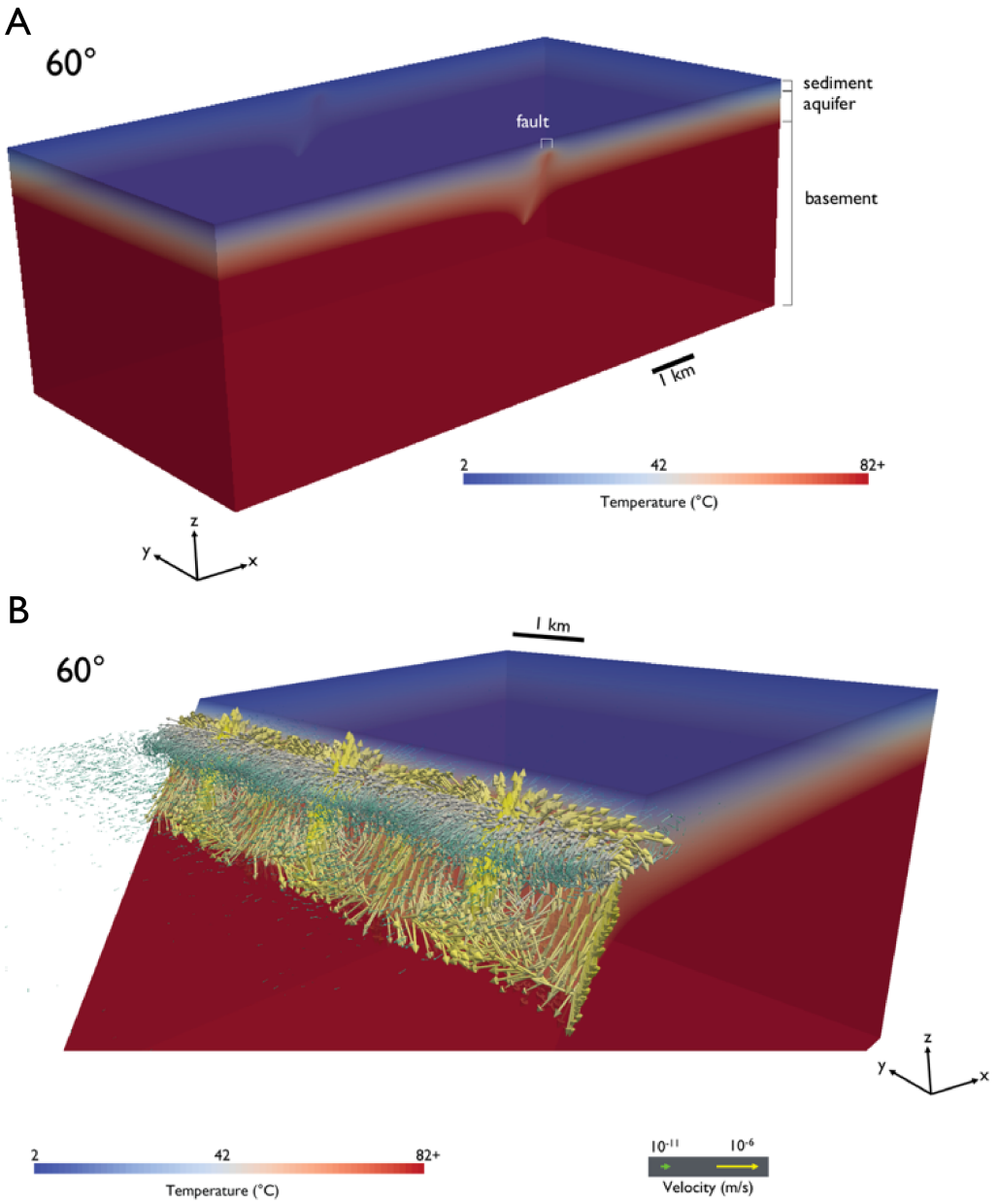

Figure 6. Contour map of the dip-parallel component of velocity in the fault , interpolated on a plane oriented perpendicular to fault dip, halfway between the top and bottom of the fault (nominal intersection depth = 500 m below sediment-rock interface). Results are at dynamic steady state for a 60° fault with $k_{aq} = 10^{-13}$ m^2 and $k_f = 10^{-11}$. Positive values indicate flow up dip; negative values indicate flow down dip. There are three convective upwellings (yellow) and four convective downwellings (dark blue).

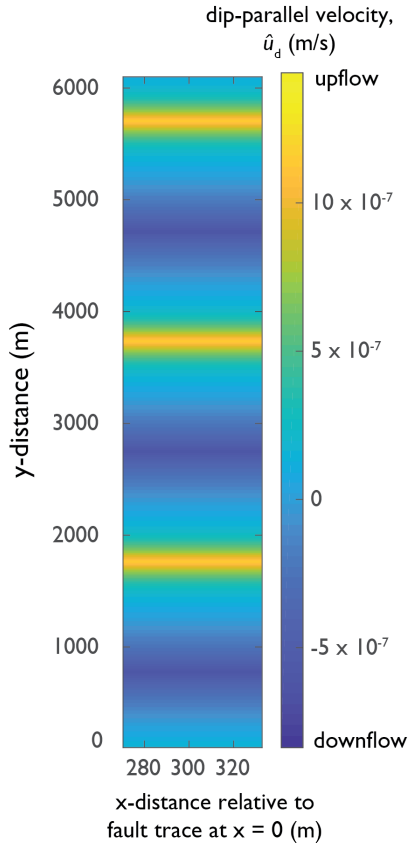

Figure 7. Seafloor heat flux at dynamic steady state for a 60° fault with $k_{aq} = 10^{-13}$ m^2 and $k_f = 10^{-11}$ m^2. There is a positive heat flux anomaly above the fault trace and heat flux suppression down dip. Background heat flux is 180 mW/m^2. Convective upwellings and downwellings are reflected in the peaks and troughs of the along-strike heat flux anomaly. The subtle, striped pattern in seafloor heat flux the y-direction reflects the arrangement of nodes in the mesh: node spacing is irregular only in the x-z plane, not in the y-direction.

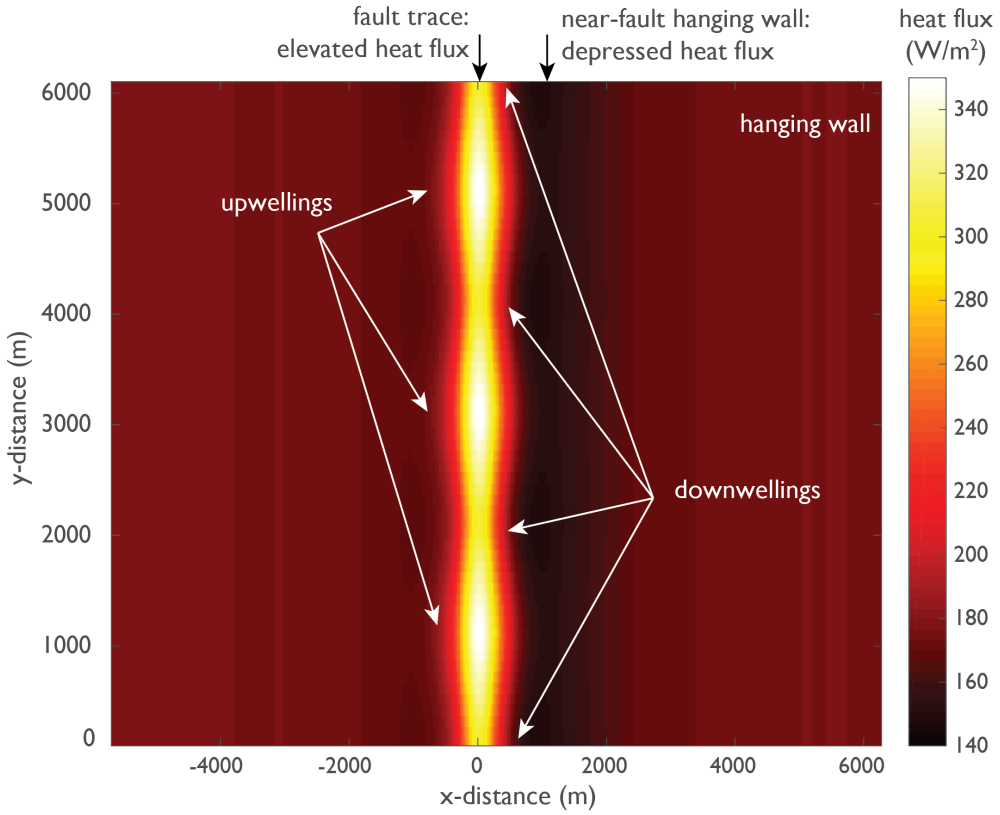

Figure 8. Seafloor heat flux results for all primary simulations with $k_{aq} = 10^{-13}$ m^2. Distance and heat flux color scales are identical to **Figure 7**.

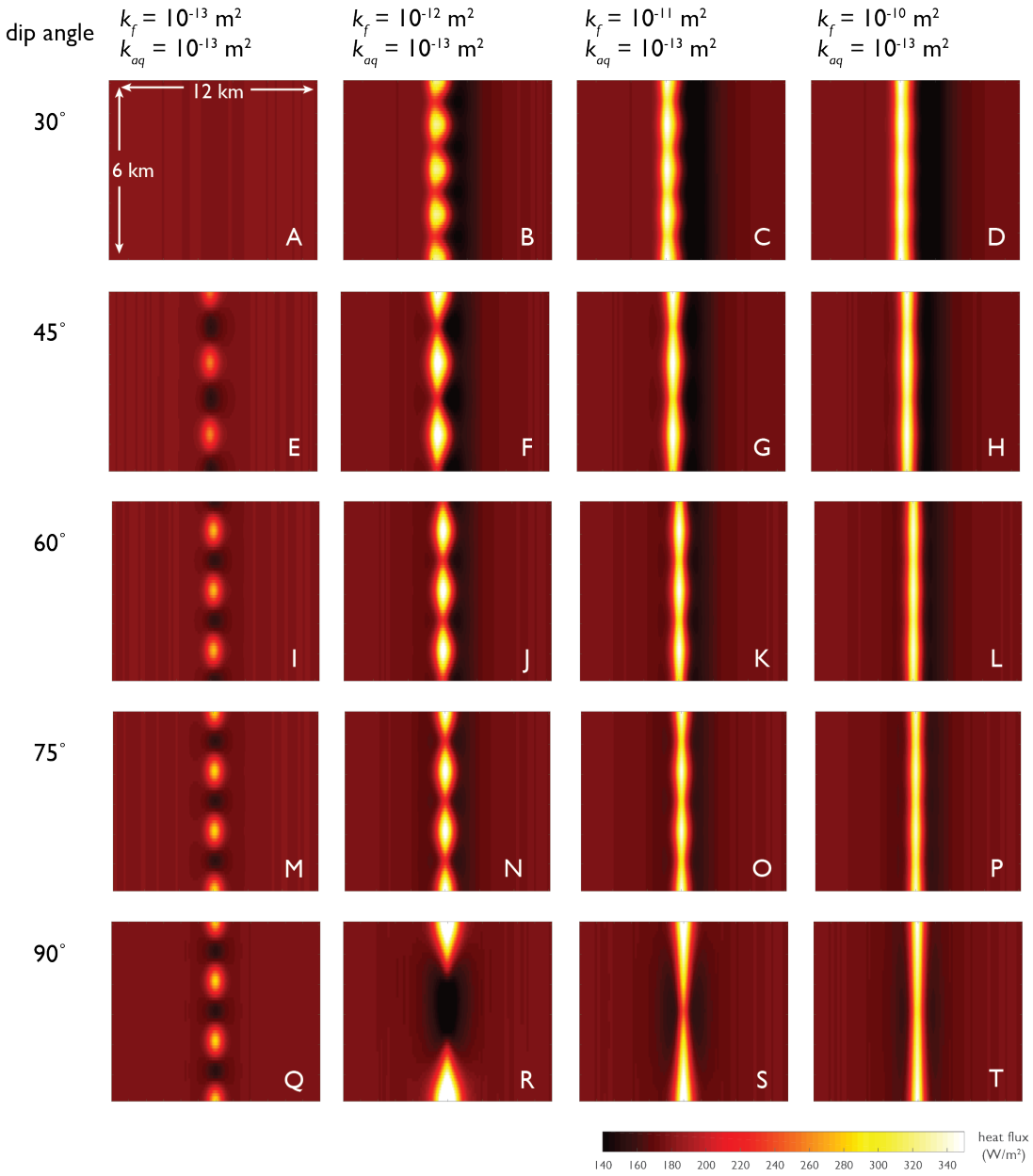

Figure 9. Number of upwellings versus dip angle for each set of k_{aq} and k_f. Triangles indicate simulations where number of upwellings is greater than number of downwellings; squares indicate number of upwellings equal to number of downwellings; inverted triangles number of upwellings less than number of downwellings.

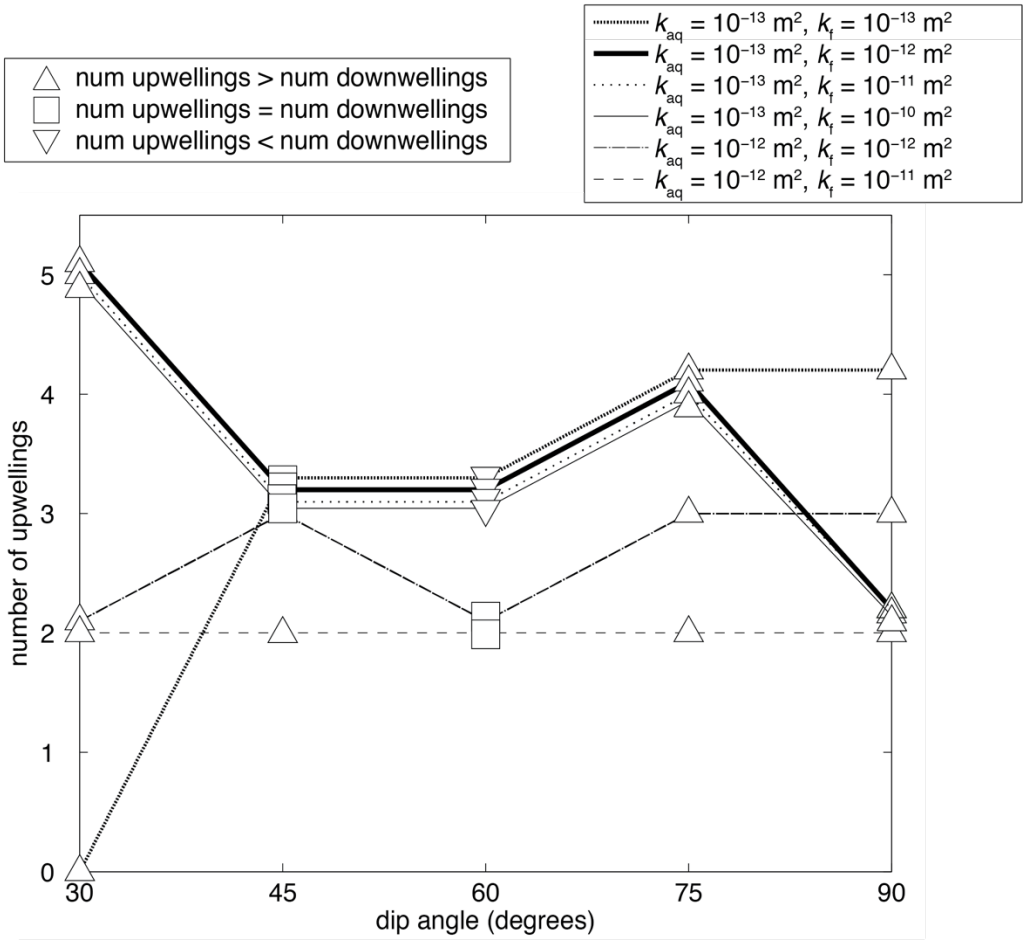

Figure 10. Seafloor heat flux results for all primary simulations with $k_{aq} = 10^{-12}$ m^2. Distance and heat flux color scales are identical to **Figure 7**.

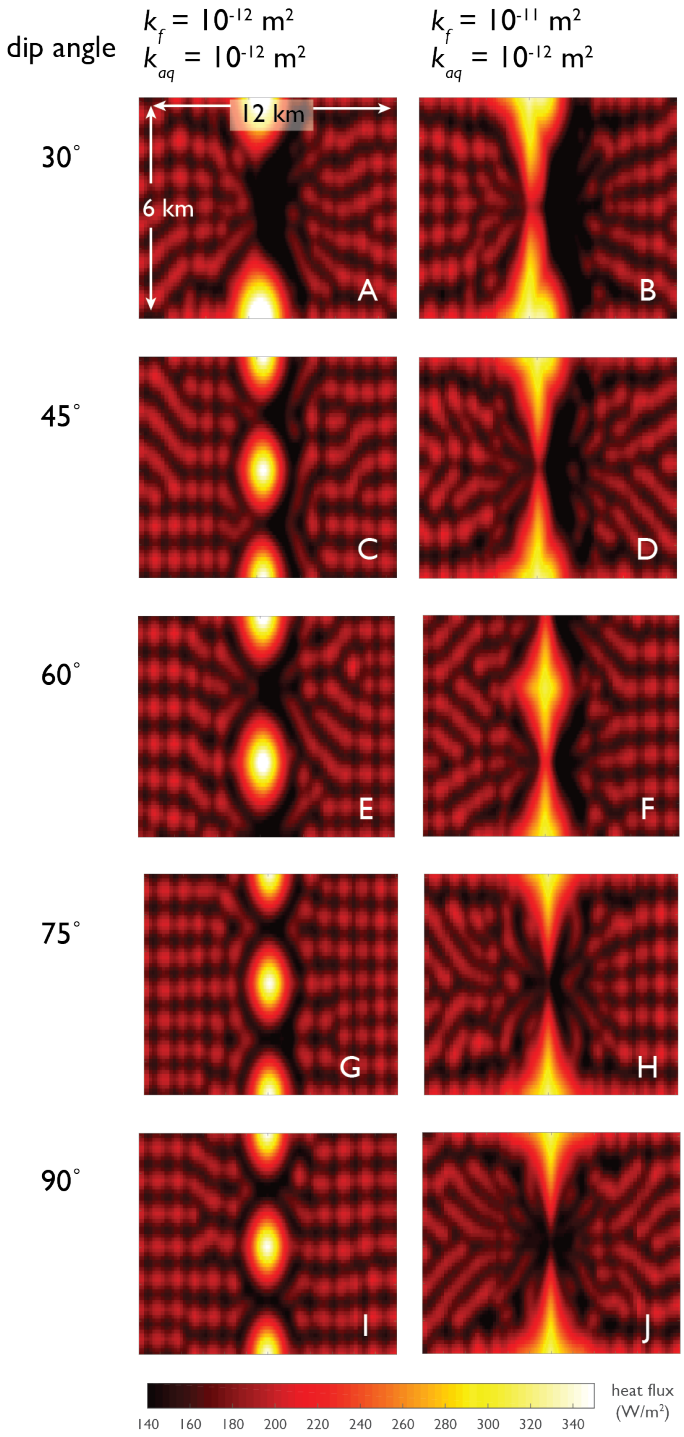

Figure 11. a. Median up-dip velocity ($\hat{u}_d$) versus dip angle for all primary simulations with $k_{aq} = 10^{-13}$ m^2. **b.** Median up-dip velocity ($\hat{u}_d$) versus dip angle for all primary simulations with $k_{aq} = 10^{-12}$ m^2.

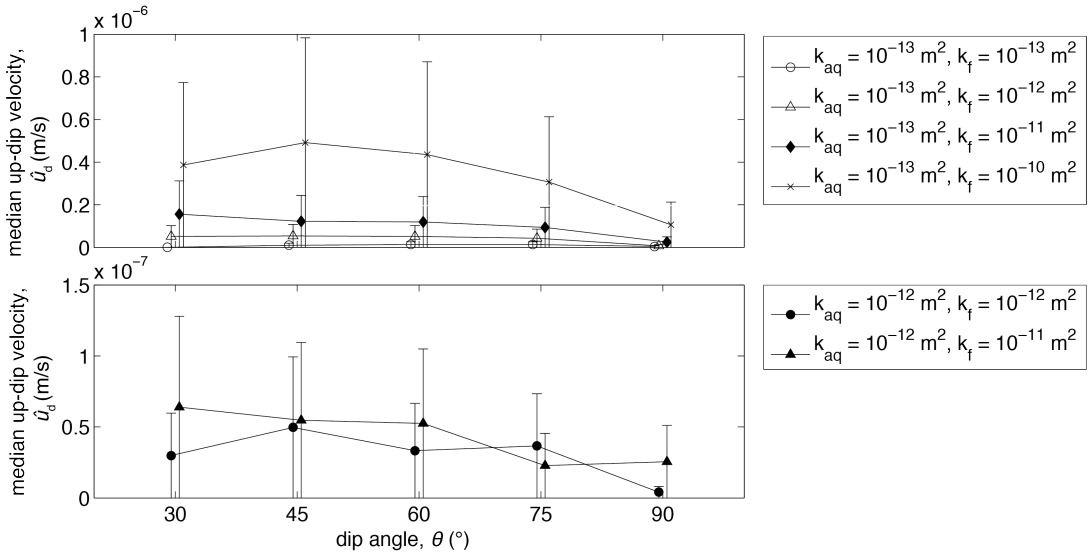

Figure 12. Median total velocity in the fault (v_f) and median total velocity in the aquifer (v_{aq}) versus permeability contrast (k_f/k_{aq}). The shaded region denotes the range of v_{aq} in simulations with no fault for $k_{aq} = 10^{-13}$ and 10^{-12} m^2. For simulations with k_f/k_{aq}, Spearman's rank correlation coefficient for v_f versus k_f/k_{aq} (R_f) is 0.97, a positive correlation significant at the .05 level. For the same set of simulations, Spearman's rank correlation coefficient for v_{aq} versus k_f/k_{aq} (R_f) is -0.32, which is not significant at the .05 level.

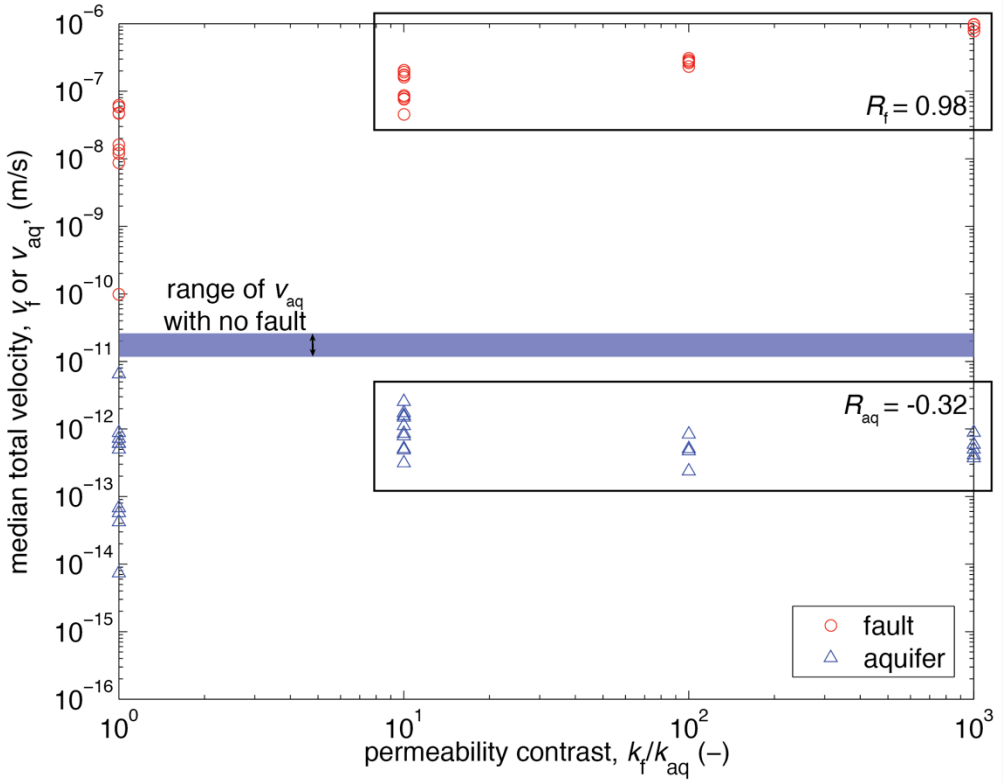

Figure 13. a. Histogram of total velocity vector magnitudes in the fault and aquifer for a 60° fault with $k_{aq} = 10^{-13}$ m^2 and $k_f = 10^{-11}$ m^2. Median values are marked with arrows. **a.** Histogram of total velocity vector magnitudes in the fault and aquifer for a 60° fault with $k_{aq} = 10^{-12}$ m^2 and $k_f = 10^{-11}$ m^2. Median values are marked with arrows. The distribution of aquifer velocity is unimodal, compared with the bimodal distribution in **a**.

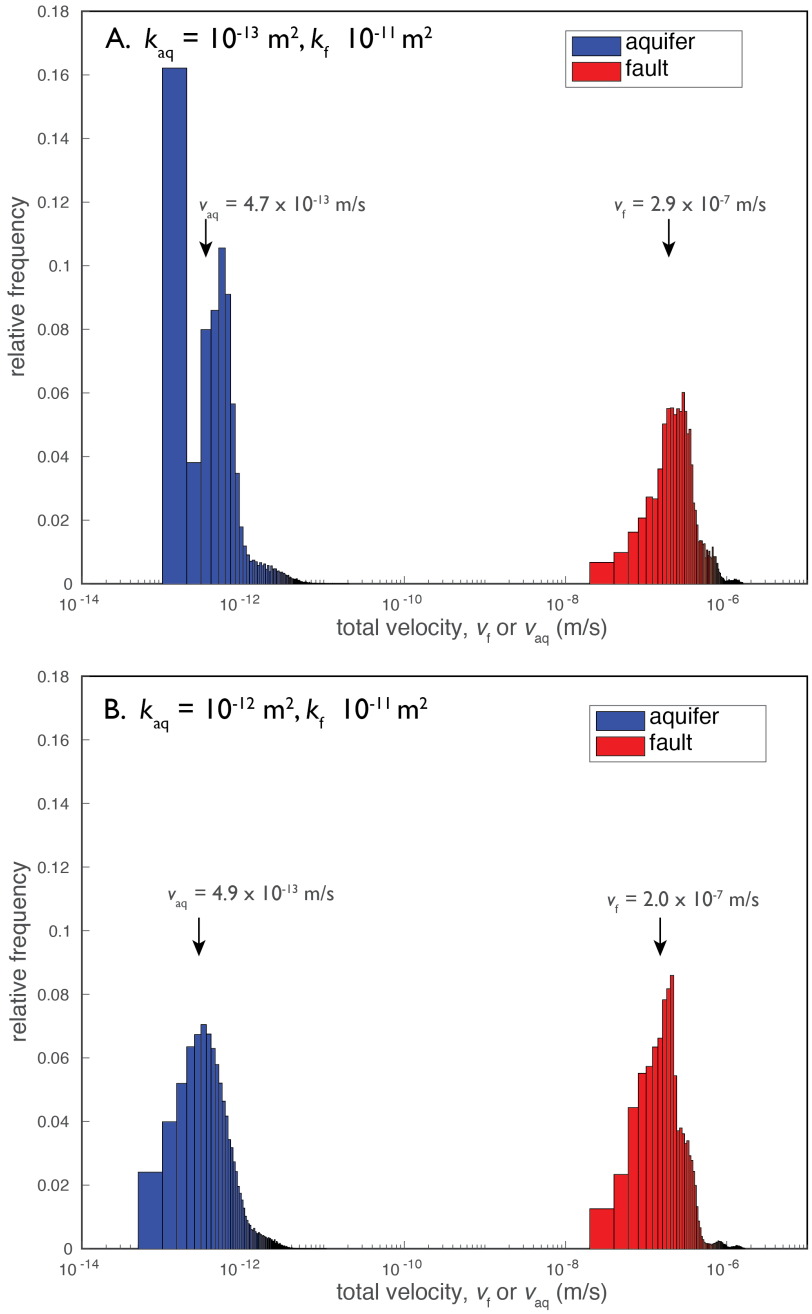

Figure 14. Heat flux fraction (HFF) versus x-distance on transects perpendicular to fault strike over upwelling heat flux peaks on the fault trace (located at x ~0). Shaded region denotes the 5% deviation from the regional background that might be reliably detected in the field. There is a peak in HFF above the fault trace for all simulations and a trough in HFF down dip when $k_{aq} = 10^{-13}$ m^2 **a.** Transects for all dip angles and $k_{aq} = 10^{-13}$ m^2 and $k_f = 10^{-11}$ m^2. **b.** Transects for all k_f values and $k_{aq} = 10^{-13}$ m^2 with a 60° fault. **b.** Transects for all k_f values and $k_{aq} = 10^{-12}$ m^2 with a 60° fault.

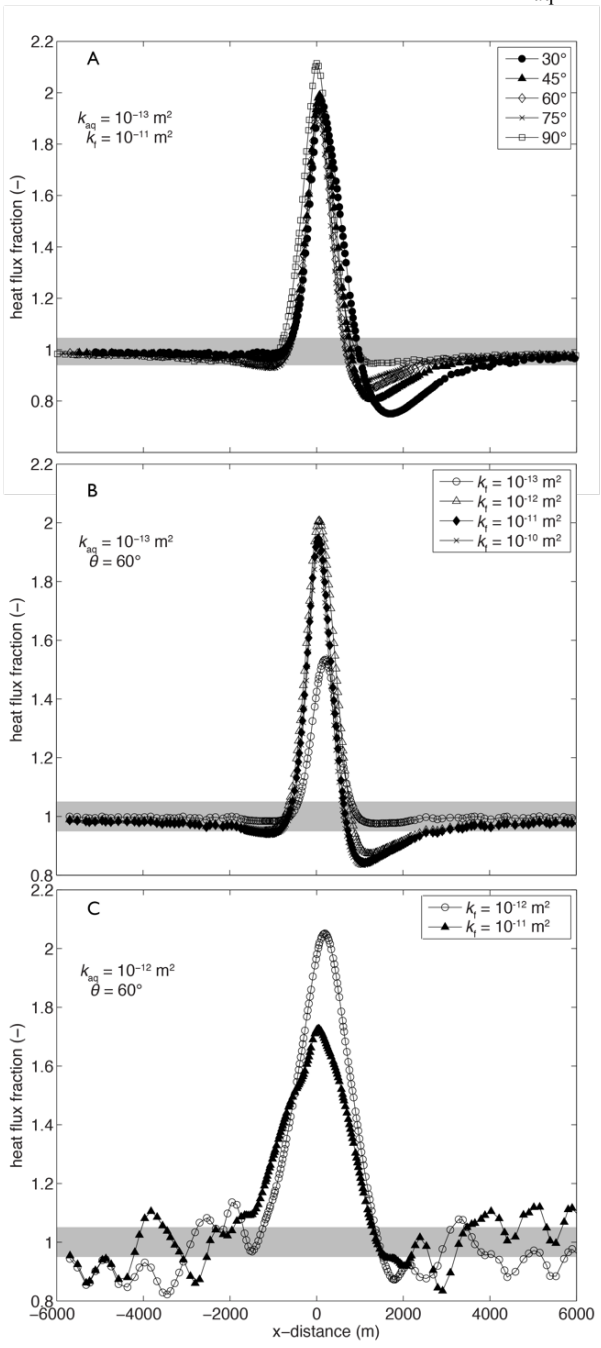

Figure 15. Seafloor heat flux results for $d_f = 3$ km and $d_f = 1$ km with $k_{aq} = 10^{-13}$ m^2 and $k_{aq} = 10^{-12}$ m^2. Distance and heat flux color scales are identical to **Figure 7**.

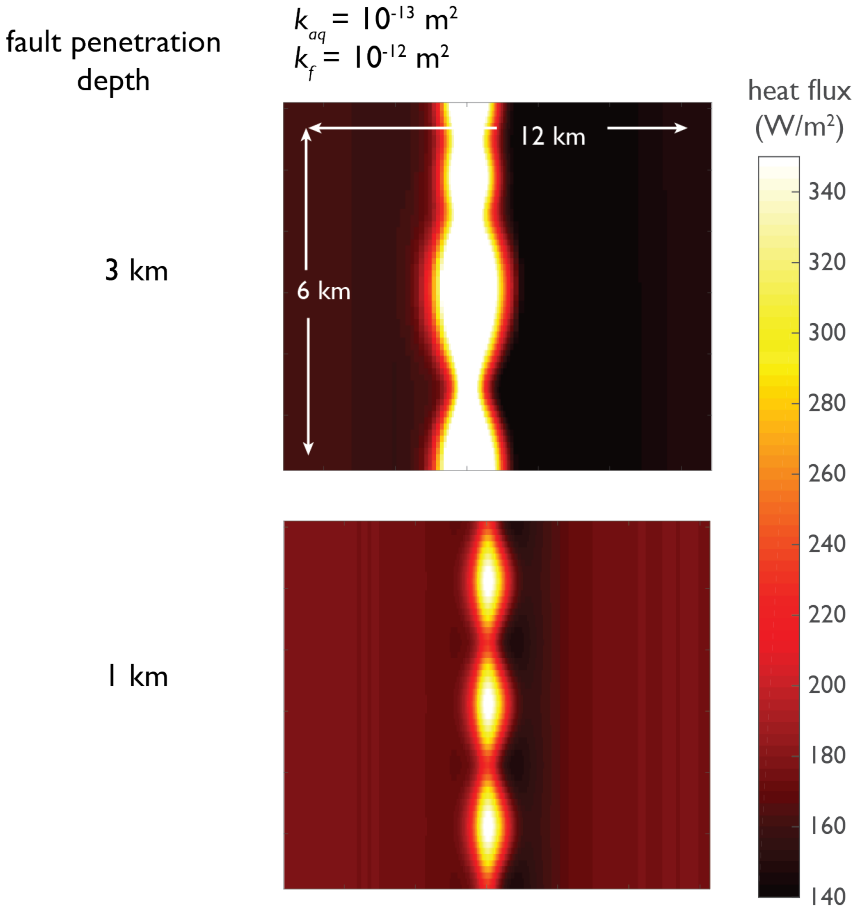

Figure 16. Three-dimensional patterns of hydrothermal circulation aquifer for a 60° fault with d_f = 3 km, $k_{aq} = 10^{-13}$ m^2 and $k_f = 10^{-12}$ m^2. Flow vectors are plotted on a natural-log scale. The hanging wall has been removed to make flow vectors more visible.

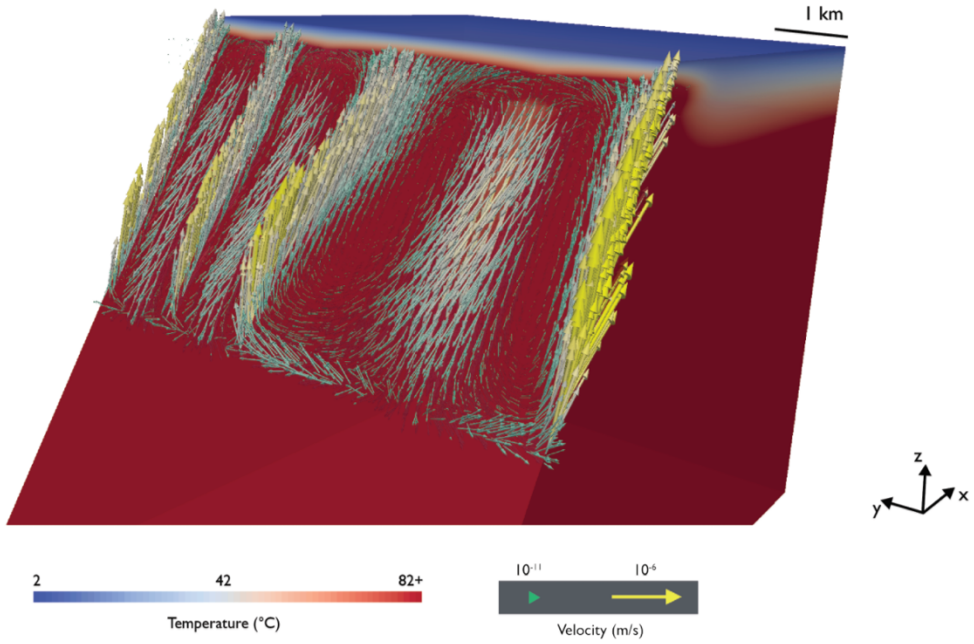

Figure 17. Heat flux fraction (HFF) versus x-distance on transects perpendicular to fault strike over upwellings and downwellings on the fault trace (located at x ~0) for a 60° fault with $k_{aq} = 10^{-13}$ m^2 and $k_f = 10^{-12}$ m^2, $d_f = 1$ km and 3 km. Shaded region denotes the 5% deviation from the regional background that might be reliably detected in the field.

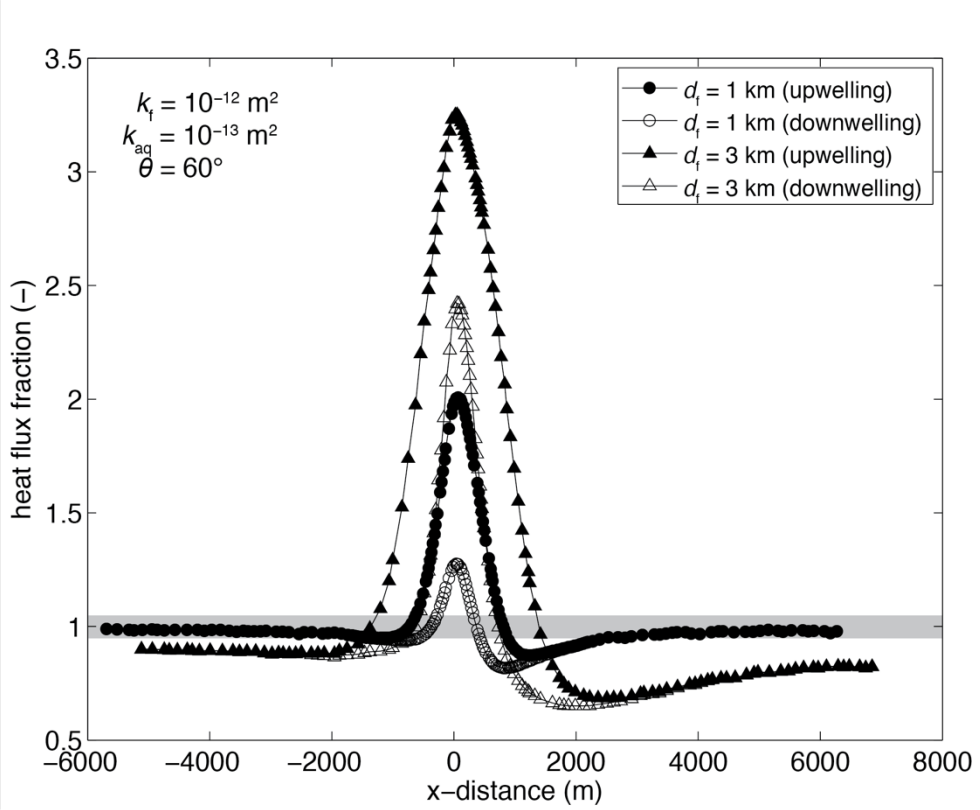

Figure 18. Seafloor heat flux results for t_f = 10 m, 30 m, and 90 m for a 60° fault with $k_{aq} = 10^{-13}$ m^2 and $k_{aq} = 10^{-12}$ m^2. Distance and heat flux color scales are identical to **Figure 7**.

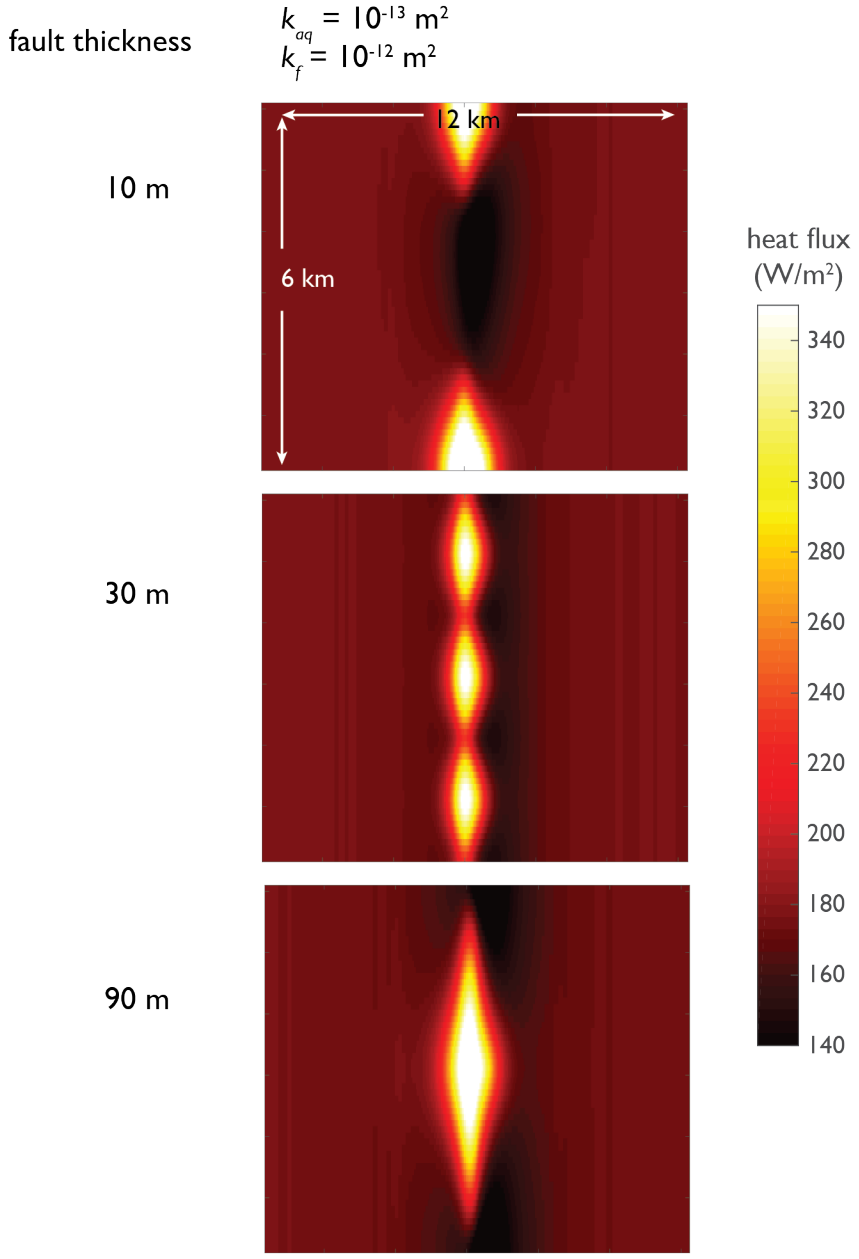

Figure 19. Heat flux fraction (HFF) versus x-distance on transects perpendicular to fault strike over upwelling heat flux peaks on the fault trace (located at x ~0) for a 60° fault with $k_{aq} = 10^{-13}$ m^2 and $k_{aq} = 10^{-12}$ m^2, t_f = 10 m, 30 m, and 90 m. Shaded region denotes the 5% deviation from the regional background that might be reliably detected in the field.

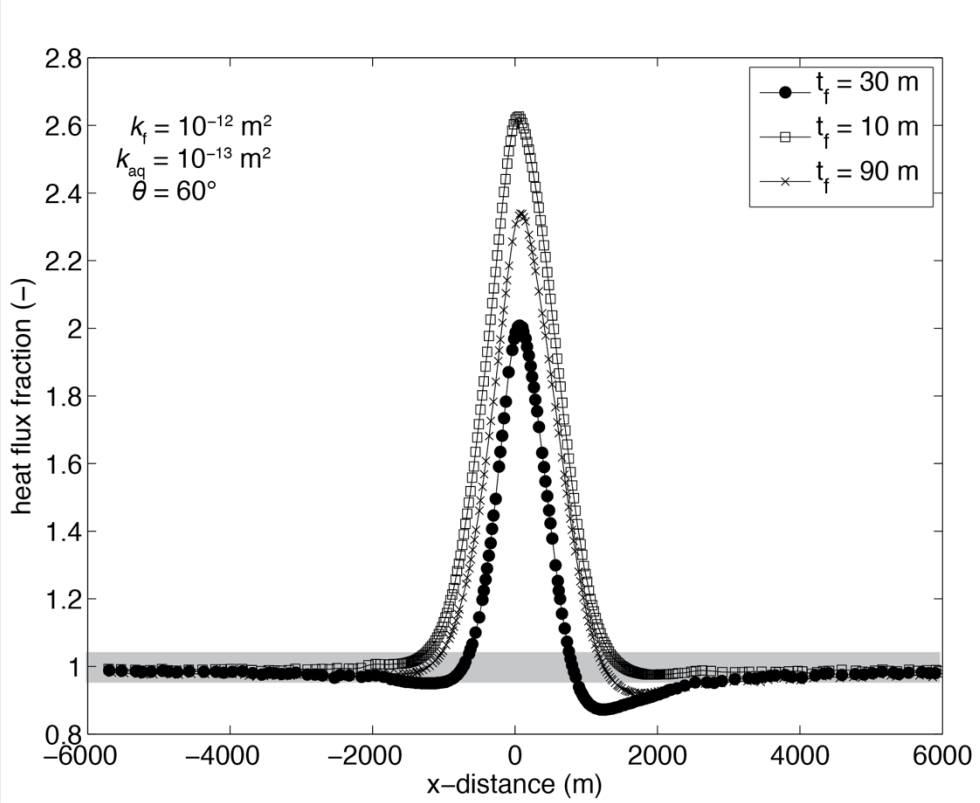

Figure 20. Seafloor heat flux results for t_{aq} = 300 m and 600 m for a 60° fault with k_{aq} = 10^{-13} m^2 and k_{aq} = 10^{-12} m^2, k_{aq} = 10^{-13} m^2 and k_{aq} = 10^{-11} m^2, k_{aq} = 10^{-12} m^2 and k_{aq} = 10^{-11} m^2. Distance and heat flux color scales are identical to **Figure 7**.

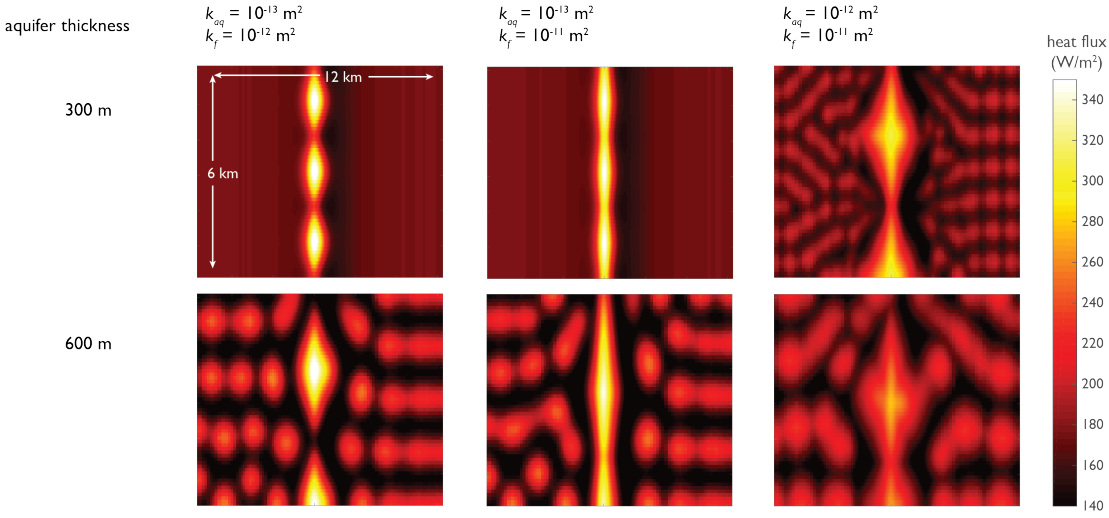

Figure 21. Heat flux fraction (HFF) versus x-distance on transects perpendicular to fault strike over upwelling heat flux peaks on the fault trace (located at x ~0). **a.** Transects for t_{aq} = 300 m and 600 m and $k_{aq} = 10^{-13}$ m^2 and $k_f = 10^{-12}$ m^2. **b.** Transects for t_{aq} = 300 m and 600 m and $k_{aq} = 10^{-13}$ m^2 and $k_f = 10^{-11}$ m^2. **c.** Transects for t_{aq} = 300 m and 600 m and $k_{aq} = 10^{-12}$ m^2 and $k_f = 10^{-11}$ m^2.

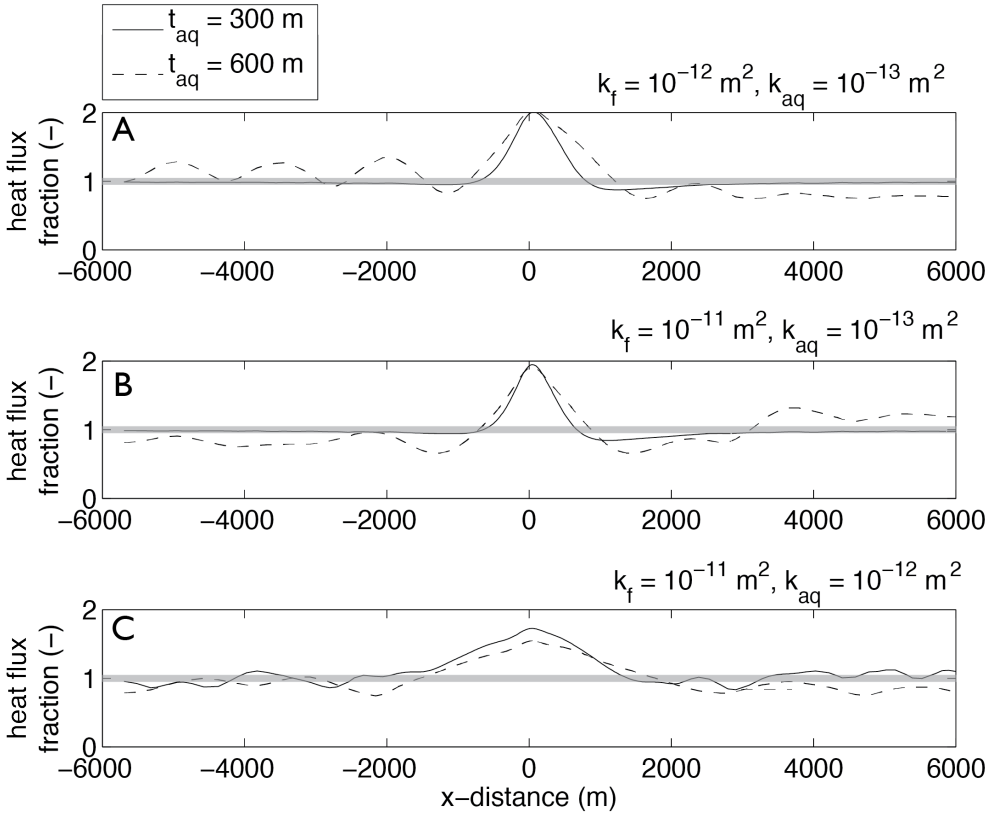

Table 1: Formation properties

	Permeability, *k* (m^2)	**Porosity, *n* (-)**	**Thermal conductivity, *λ* (W/m K)**
Sediment[a]	1.3×10^{-17} to 2.2×10^{-17}	0.41 to 0.52	1.42 to 1.51
Aquifer[b]	10^{-13} to 10^{-12}	0.1	1.82
Fault[b]	10^{-13} to 10^{-10}	0.1	1.82
Deep crust[b]	10^{-18}	0.0	2.05

[a] Values vary with depth and are the same for all simulations
[b] Values are homogeneous in each region

Table 2: Geometry and property ranges used in "primary" dip angle and permeability study. Reference simulation parameters are bolded.

Dip angle, θ (°)	Aquifer thickness, t_{aq} (m)	Fault thickness, t_f (m)	Fault depth, d_f (m)	Aquifer permeability, k_{aq} (m^2)	Fault permeability, k_f (m^2)
30	300	30	1000	10^{-13}, 10^{-12}	10^{-13}, 10^{-12}, 10^{-11}, 10^{-10}
45	300	30	1000	10^{-13}, 10^{-12}	10^{-13}, 10^{-12}, 10^{-11}, 10^{-10}
60	300	30	1000	10^{-13}, 10^{-12}	10^{-13}, 10^{-12}, 10^{-11}, 10^{-10}
75	300	30	1000	10^{-13}, 10^{-12}	10^{-13}, 10^{-12}, 10^{-11}, 10^{-10}
90	300	30	1000	10^{-13}, 10^{-12}	10^{-13}, 10^{-12}, 10^{-11}, 10^{-10}

Table 3: Geometry and property ranges used in "secondary" simulations

Dip angle, θ (°)	Aquifer thickness, t_{aq} (m)	Fault thickness, t_f (m)	Fault depth. d_f (m)	Aquifer permeability, k_{aq} (m^2)	Fault permeability, k_f (m^2)
60	600	30	1000	10^{-13}, 10^{-12}	10^{-13}, 10^{-12}, 10^{-11}
60	300	10	1000	10^{-13}	10^{-12}
60	300	90	1000	10^{-13}	10^{-12}
60	300	30	3000	10^{-13}	10^{-12}

Table 4: Results for d_f = 1 km and 3 km, $k_{aq} = 10^{-13}$ m^2, $k_f = 10^{-12}$ m^2, = 60°

Fault depth, d_f (m)	Median up-dip velocity, $\hat{u}_d$ (m/s)	Median total velocity in fault, v_f (m/s)	Median total velocity in aquifer, v_{aq} (m/s)
1000	1.3×10^{-7}	8.3×10^{-8}	3.1×10^{-13}
3000	3.7×10^{-7}	2.8×10^{-7}	4.6×10^{-12}

Table 5: Results for t_f = 10 m and 90 m, $k_{aq} = 10^{-13}$ m^2, $k_f = 10^{-12}$ m^2, = 60°

Fault thickness, t_f (m)	Median up-dip velocity, $\hat{u}_d$ (m/s)	Median total velocity in fault, v_f (m/s)	Median total velocity in aquifer, v_{aq} (m/s)
10	4.1×10^{-8}	7.1×10^{-8}	4.8×10^{-13}
90	2.2×10^{-8}	4.5×10^{-8}	6.5×10^{-12}

Table 6: Results for t_{aq} = 600 m, t_f = 30 m, d_f = 1 km, = 60°

Aquifer thickness, t_{aq} (m)	Fault permeability, k_f (m^2)	Aquifer permeability, k_{aq} (m^2)	Median up-dip velocity, $\hat{u}_d$ (m/s)	Median total velocity in fault, v_f (m/s)	Median total velocity in aquifer, v_{aq} (m/s)
600	10^{-12}	10^{-13}	4.1×10^{-8}	5.3×10^{-8}	2.0×10^{-12}
600	10^{-11}	10^{-13}	5.3×10^{-8}	2.0×10^{-7}	1.3×10^{-12}
600	10^{-11}	10^{-12}	6.3×10^{-8}	1.4×10^{-7}	6.6×10^{-13}

Table 7: Heat flux fractions (*HFF*) for t_f = 10 m, 30 m, and 90 m, $k_{aq} = 10^{-13}$ m^2, $k_f = 10^{-12}$ m^2, = 60°. H_f is defined in the text.

Fault thickness, t_f (m)	Positive heat flux anomaly, *HFF* (W/m^2)
10	6.0
30	6.4
90	7.4